IOPscience iopscience.iop.org

Home Search Collections Journals About Contact us My IOPscience

Squeeze-out and wear: fundamental principles and applications

This article has been downloaded from IOPscience. Please scroll down to see the full text article.

2004 J. Phys.: Condens. Matter 16 R295

(http://iopscience.iop.org/0953-8984/16/10/R01)

View the table of contents for this issue, or go to the journal homepage for more

Download details:
IP Address: 129.252.86.83
The article was downloaded on 27/05/2010 at 12:48

Please note that terms and conditions apply.

INSTITUTE OF PHYSICS PUBLISHING JOURNAL OF PHYSICS: CONDENSED MATTER

J. Phys.: Condens. Matter **16** (2004) R295–R355 PII: S0953-8984(04)35473-1

**TOPICAL REVIEW**

# Squeeze-out and wear: fundamental principles and applications

**B N J Persson**[1] **and F Mugele**[2]

[1] Institut für Festkörperforschung, Forschungszentrum Jülich, FZ-Jülich, 52425 Jülich, Germany
[2] Applied Physics Department, University of Ulm, 89081 Ulm, Germany

Received 23 May 2003
Published 27 February 2004
Online at
stacks.iop.org/JPhysCM/16/R295 (DOI: 10.1088/0953-8984/16/10/R01)

**Abstract**

The dynamics of squeeze-out of thin liquid films between two solids is perhaps the most central topic in tribology. It is directly relevant for wear and indirectly involved in many other important processes, e.g., adhesion and friction. In this review we present a broad overview of the basic principles of squeeze-out, and present a number of applications to adhesion, friction and wear. We first describe the squeezing of 'thick' liquid films (thickness larger than ∼100 Å), which can be described using the Navier–Stokes equations of hydrodynamics, and present experimental illustrations for soft solids (rubber) and hard solids (mica). Next we consider molecularly thin liquid films. Here the squeeze-out occurs in a quantized manner involving a monolayer at each step. We discuss the nature of the nucleation of $n \rightarrow n-1$ monolayer squeeze-out, where $n$ is the number of trapped monolayers. We consider in detail the nature of the spreading which follows the nucleation and show that the boundary line may exhibit instabilities. Sometimes the squeeze-out is incomplete, resulting in trapped islands. These islands may be pinned, or else they drift slowly to the periphery of the contact area where they get squeezed out through narrow liquid channels. We consider also dewetting at soft interfaces and present an application to the adhesion of soft objects on wet substrates. Finally, we present molecular dynamics and kinetic Monte Carlo simulation results on various aspects of squeeze-out for liquid-like and solid-like lubrication films, and discuss the implications for wear.

(Some figures in this article are in colour only in the electronic version)

## Contents

1. Introduction 296
2. Experimental considerations 299

 © 2004 IOP Publishing Ltd Printed in the UK 

3. 3D hydrodynamic squeeze-out 301
3.1. Basic principles 301
3.2. Elastohydrodynamics 302
3.3. Experimental results 303
4. Squeezing molecularly thin 2D liquid-like films 306
4.1. Nucleation 306
4.2. Spreading 309
4.3. Boundary line instability 314
4.4. Motion of trapped island 318
4.5. Role of the 2D lubricant compressibility 324
4.6. Role of the perpendicular pressure 325
4.7. Dewetting of soft interfaces 327
4.8. Adhesion of a soft object on a wet substrate 333
4.9. Adhesion in biological systems 333
4.10. Droplet shape, contact angle and Laplace pressure 334
4.11. Squeezing wetting and nonwetting fluids films 336
4.12. A hair-care application: conditioners and the combing of wet hair 340
5. Squeezing molecularly thin 2D solid-like films 342
5.1. Atomic lubricants 345
5.2. Linear hydrocarbons 347
6. Relation between squeeze-out and wear 351
7. Outlook 353
Acknowledgments 353
References 354

## 1. Introduction

Tribology, the science of interacting solid surfaces in relative motion, is one of the oldest problems in physics, and has undoubtedly a huge practical importance [1–4]. In recent years, the ability to produce durable low friction surfaces and lubricants has become an important factor in the miniaturization of moving components in technologically advanced devices. For such applications, the interest is focused on the stability under pressure of thin lubricant films, since the complete squeeze-out of the lubricant from an interface may give rise to cold-welded junctions, resulting in high friction and catastrophically large wear.

Consider the following generic situation: an elastic ball squeezed against a rigid flat substrate in a fluid; see figure 1. As long as the separation between the two solids is larger than, say, 1000 Å, the fluid squeeze-out can usually be described using the Navier–Stokes equations of hydrodynamics with classical no-slip boundary conditions. At this level, specific interactions between liquid and solid are ignored, the solid walls are assumed to be perfectly smooth and rigid, and the liquid is treated as a structureless continuum. As the film thickness decreases below ∼1000 Å these assumptions progressively fail. Initially the solid–liquid interactions, and the surface roughness, mainly affect the validity of the no-slip boundary condition. Violation of this condition was first observed in polymer systems [5]. However, more recently experiments also demonstrated the occurrence of slip in simple liquids [6–10]. Although a final consensus on the range of slip has yet to be reached, it is now clear that a detailed understanding of this problem requires a careful consideration of the interplay between surface roughness and the wall–lubricant interaction, in particular the lateral corrugation of the interaction potential.

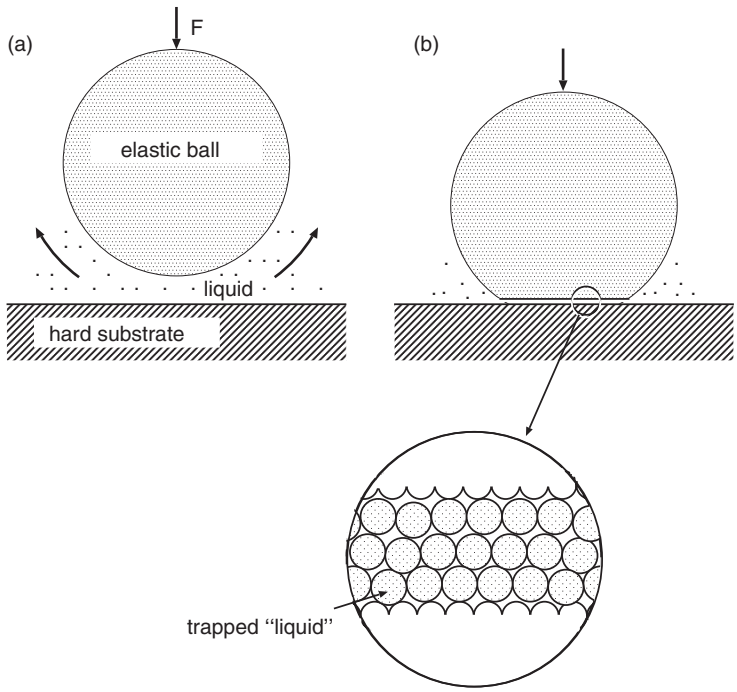


**Figure 1.** Squeezing a liquid between an elastic ball and a flat hard substrate. (a) As long as the separation between the ball and the substrate is large enough, the liquid is squeezed out in accordance with the standard equations of hydrodynamics. For short ball–substrate separation, the solid deforms elastically. If the squeezing force $F$ is below some critical value, a thin slab of lubricant fluid may be trapped between the solid bodies, often resulting in low friction and negligible wear.

In the present review, we focus on the breakdown of the two remaining approximations mentioned above, namely the perfect rigidity of the solid walls and—in particular—the continuum description of the liquid. When the separation between the surfaces is decreased to a few molecular diameters, the motion of the ball may stop with a finite number of molecular layers of lubricant trapped at the interface. It has been shown both experimentally and theoretically that when simple fluids (quasi-spherical molecules and linear hydrocarbons) are confined between atomically flat surfaces at microscopic separations, the behaviour of the lubricant is mainly determined by the presence of the hard walls, that induce layering in the perpendicular direction [11–18]. The thinning of the lubrication film under applied pressure occurs stepwise, by expulsion of individual layers. Figure 2 illustrates the transition from continuous hydrodynamic behaviour at large separations, to discrete stepwise expulsion within the range of liquid layering. These layering transitions appear to be thermally activated [19–25]. The appearance of layering and layering transitions is not restricted to simple molecular liquids. Rather, it is a very general phenomenon related to the breaking of symmetry at smooth interfaces. For instance, layering transitions were also observed in soap films containing various sorts of colloidal particles, micelles, or even complex networks of polyelectrolytes [26–29].

While layering of the molecules perpendicular to the pore walls is well established both experimentally and from simulations, much less in known about the in-plane structure. Attempts to determine the structure using x-ray scattering have so far been limited to rather larger film thickness ($>$100 nm) [30, 31] because the scattering signal from just a few

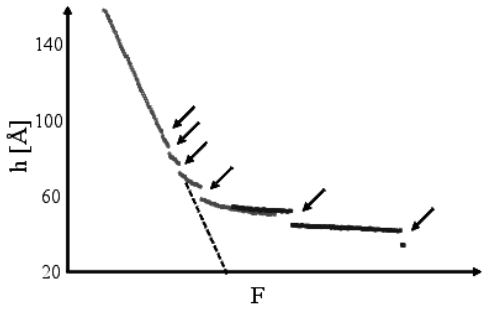


**Figure 2.** Variation of the thickness $h$ of a simple film (OMCTS) during a linear increase of the squeezing force $F$. Note the transition from a continuous decrease of $h$ at large separation to a discrete stepwise behaviour (arrows) at small separations [49].

monolayers of material was too weak. However, friction force measurements showed a finite shear strength along with typical solid-like stick–slip friction in a number of experiments with simple liquids. This observation was interpreted as a sign of either confinement induced solidification or confinement induced viscosity enhancement [11, 12, 15–18, 32, 33]. Some of these observations were subsequently reproduced in numerical simulations. It was also pointed out that there should be a fundamental difference between simple non-associating liquids and water. The fact that water expands upon freezing was reported to stabilize the liquid phase under confinement and under pressure [33–37]. However, it was argued (and in some cases clearly demonstrated) that trace amounts of contamination either within the liquid [15–18, 33, 35] or on the surfaces [38–43] may have a tremendous effect on the frictional behaviour. A consistent picture has yet to emerge. In the present review, we focus on situations where the confined material behaves in a liquid-like way (sections 3 and 4). Confinement induced solidification will only be addressed in the context of numerical simulations (section 5).

Although liquid layering has been studied for more than 20 years using the surface forces apparatus (SFA), the dynamics of squeeze-out was investigated for the first time only recently [44]. By modifying the conventional SFA set-up [45], it was possible to image the lateral variation of the gap between the two anvil surfaces as a function of time. These experiments addressed the $n = 1 \rightarrow 0$ transition for a straight chain alcohol. More recently, in a refined experimental set-up, we were able to image several layering transitions in great detail [41, 46] for octamethyltetrasiloxane (OMCTS), which is widely used as a model lubricant.

The basic theory of 2D squeeze-out dynamics of 2D liquid-like lubrication films was outlined in [19]. Initially the system is trapped in a metastable state at the initial film thickness. Squeeze-out starts by a thermally activated nucleation process in which a density fluctuation forms a small hole. Once it has formed, a 2D pressure difference develops between the boundary line separating the squeezed out region from the rest of the system, and the outer (roughly circular) boundary line of the contact area, thus driving out the rest of the 2D fluid.

The phenomenology of layering transitions in 2D solid-like boundary lubrication has been studied in [37, 47, 48]. It has been shown in a series of computer simulations that for solid-like layers, layering transitions are sometimes initiated by a disordering transition, after which the lubricant behaves in a liquid-like manner for the rest of the squeeze-out process.

This review is organized as follows. In section 2 we describe the experimental method which has been used to obtain most of the experimental results discussed in this review. Section 3 reviews the basic theory of hydrodynamic and elastohydrodynamic squeeze-out,

and presents experimental results for soft solid walls (rubber) and harder walls (mica sheets). Section 4 presents an extensive discussion about the squeezing of molecularly thin, 2D liquid-like films. Experimental and theoretical results are presented both for the nucleation of squeeze-out and for the squeeze-out dynamics. We also consider the dewetting of soft interfaces and present applications to adhesion in biological systems, and to hair-care. In section 5 we consider the squeezing of molecularly thin, 2D solid-like films. This topic is studied using molecular dynamics as no analytical approach has been presented so far. We consider both atomic lubricants and hydrocarbons. In section 6 we present experimental results related to wear, and show how some of the observations can be explained on the basis of the theoretical results for squeeze-out. The review ends with a summary and an outlook.

## 2. Experimental considerations

The squeeze-out of liquid from the gap between macroscopic elastic balls and flat walls, as sketched in figure 1, has been investigated in great detail in classical work on lubrication. Here, we are interested in the behaviour of lubricant layers with a thickness of only a few molecular diameters. In order to be able to define the separation between two solid surfaces with this accuracy, the surfaces must be sufficiently smooth on the lateral scale of the contact area. Experimentally there are essentially two ways to achieve such a situation. Either one addresses a situation with an extremely small contact area or one works with single-crystal surfaces, which are atomically smooth on a macroscopic lateral scale. The former approach is realized in the atomic force microscope (AFM), the latter in a SFA.

In an AFM, one surface is sharp tip with a typical radius of curvature of a few nanometres. Due to the sharpness of the tip, the opposing sample surface needs to be flat only on a lateral scale of several nanometres. The sharpness of the tip also implies that the pressure in the contact area is rather high, typically of the order of GPa. Furthermore, only a relatively small number of molecules are affected by the geometric confinement. Nevertheless, molecular layering has been observed in AFM measurements for a variety of simple liquids [50–52]. One goal of these measurements—beyond studying the geometric arrangement of the molecules—was to determine the threshold forces required to squeeze out individual liquid layers (see section 4.1 [23–25]). The squeeze-out process of molecular layers itself was too fast to be detected.

More experimental knowledge about confined liquid films stems from measurements using the SFA. A typical set-up is shown schematically in figure 3. The key part is two atomically smooth mica sheets glued to cylindrical lenses (radius of curvature $\sim$1 cm) with their axes perpendicular to each other. Upon bringing the cylindrical lenses together, the two opposing mica surfaces touch at a well defined single contact point. If the pressure is increased, the surfaces deform elastically. This gives rise to a contact area with a diameter ranging from a few micrometres to several tens of micrometres, depending on the pressure and the effective elasticity of the substrate (mica plus underlying glue). Mica surfaces can be prepared to be atomically smooth on this and in fact even on much larger lateral scales. If the surfaces are pressed together in a liquid environment, a thin film is typically trapped between them. In order to permit the measurement of the thickness of this layer, the backs of the mica substrates are coated with silver layers. The two mirrors form a Fabry–Perot interferometer, which allows an interferometric measurement of the liquid film thickness with a resolution of the order of 1 Å. Since one of the mica surfaces is mounted on a cantilever spring, one can record force–distance curves, as in atomic force microscopy (see figure 2). Since the force between two crossed cylinders (in the absence of significant elastic deformation) is proportional to the interaction energy per unit area of two planar substrates, these measurements have been used extensively to study the equilibrium properties of confined liquid films [11].

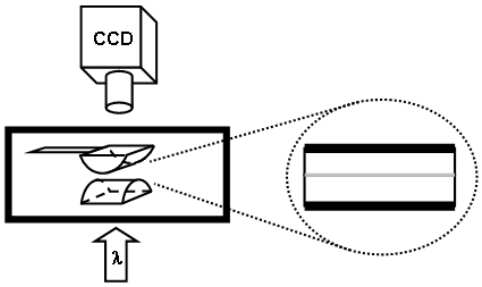


**Figure 3.** The schematic set-up of a surface forces apparatus (SFA) consisting of two cylindrical lenses mounted in crossed cylinder geometry inside a sealed container. The sample liquid fills the gap between the surfaces. Transmitted intensity is measured with a CCD camera. On the right, the contact area of the surfaces is shown in a zoomed view. Black: Ag mirrors (thickness about 50 nm); white: mica (thickness about 1 $\mu$m); grey: sample liquid (thickness about 1–10 nm).

In order to study non-equilibrium properties, two types of experiment can be performed with an SFA. The commonest approach is to shear the two substrates with respect to each other at constant film thickness and to measure the response of the liquid film [12, 15–18, 32, 35]. For the present purposes, we are more interested in experiments of the second type, namely in drainage. Here one of the surfaces is either pressed toward the other at a finite speed via a spring, or it is oscillated in the normal direction [53, 54]. In both cases, the hydrodynamic force between the surfaces is calculated from the response of the liquid film thickness to the drive. Typically, the results are compared to hydrodynamic calculations [55] similar to the one presented in the following section. Deviations between the experiments and the hydrodynamic model arise for instance if the no-slip boundary condition is violated [6–10]. Several problems are encountered if this technique is to be extended to the thickness range of a few molecular diameters, which we are interested in here. First, the force measurements average over a large area. Potential inhomogeneities on the surfaces or irregularities of the surface geometry may thus disturb the measurement [38–40]. Second, there is currently no theory available to compare the results to when conventional hydrodynamics breaks down, as the signature of individual molecular layers emerges in the measurements.

However, the SFA apparatus does not only allow one to measure forces. By a simple extension of the conventional set-up, it becomes possible to image dynamic processes in confined liquid films directly instead of inferring their properties from indirect force measurements [44–46]. Conventionally, the apparatus is illuminated with white light. The transmitted light is then decomposed into its spectral components with a monochromator. The wavelength of the transmitted light can be converted into the thickness of the liquid film. With this procedure one-dimensional thickness profiles of the liquid film and force–distance curves (see figure 2) can be obtained. If monochromatic light is used to illuminate the apparatus, the transmitted light can be recorded directly in two dimensions with a video microscope. In this case, the intensity of the transmitted light contains the film thickness information. The conversion is performed using standard procedures for thin film interferometry [45]. If the wavelength of light is chosen on the wing of one of the transmission peaks a thickness resolution of $\approx$1 Å is obtained, as in the conventional SFA technique. Depending on the mica thickness and various other experimental parameters, a change in film thickness of 1 nm typically leads to a change in transmission of 5–10%. Figure 4 shows the transmitted intensity in the centre of the contact area as the two surfaces are pressed together with continuously increasing load. A series of four consecutive layering transitions is clearly seen. Two-dimensional video images

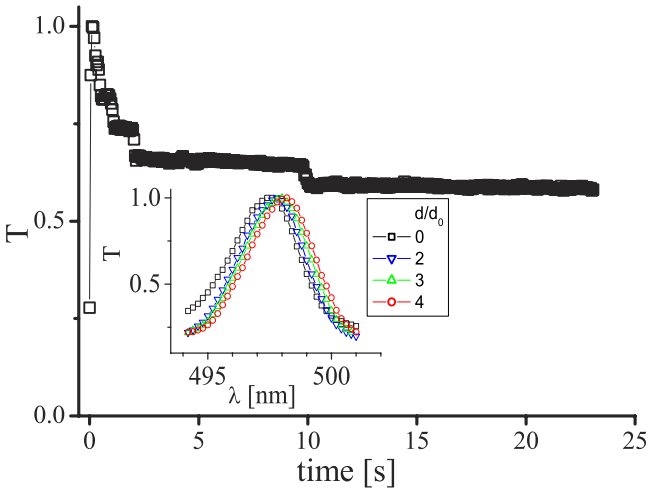


**Figure 4.** Transmitted intensity versus time averaged over a small area around the apexes of the surfaces. The load was increased continuously with time. Each step corresponds to the collapse of one molecular layer $h_0 = 0.9$ nm (incident wavelength: $\lambda = 499.2$ nm). Inset: transmitted intensity versus wavelength for constant film thickness corresponding to 1 s $< t <$ 2 s, 2 s $< t <$ 10 s and $t >$ 10 s in the main figure, respectively. Note that the collapse of a monolayer may lead to a decrease or to an increase in the transmission, depending on whether the incident wavelength is chosen on the left or on the right wing of the transmission peak.

recorded during the transitions will be presented and discussed below along with the theoretical description in section 4.2.

## 3. 3D hydrodynamic squeeze-out

### *3.1. Basic principles*

Consider two solid bodies squeezed against each other in a liquid. In the simplest case, where the elastic deformations of the bodies can be neglected, and where the liquid behaves as a Newtonian fluid, the motion of the fluid can be obtained from the Navier–Stokes equations of hydrodynamics. Assuming an incompressible fluid described by the velocity field $\mathbf{v}(\mathbf{x}, t)$ and the pressure field $P(\mathbf{x}, t)$ these equations take the form

$$\nabla \cdot \mathbf{v} = 0, \tag{1}$$

$$\frac{\partial \mathbf{v}}{\partial t} + \mathbf{v} \cdot \nabla \mathbf{v} = -\frac{1}{\rho} \nabla P + \nu \nabla^2 \mathbf{v} \tag{2}$$

where $\rho$ is the mass density and $\nu = \mu/\rho$ the kinematic viscosity of the fluid. In most cases related to squeezing, the Reynolds number $R = v_0 h/\nu \ll 1$, where $v_0$ is some characteristic velocity and $h$ some characteristic separation between the solid walls. Thus the flow is usually laminar (no turbulent flow). In most cases, when calculating the flow field, it is possible to neglect the non-linear term and the time derivative term in (2) to get

$$\nabla P = \mu \nabla^2 \mathbf{v}. \tag{3}$$

This equation, together with the continuity equation, forms the basis for most calculations of squeezing when the solids can be considered as rigid objects. A particularly simple and

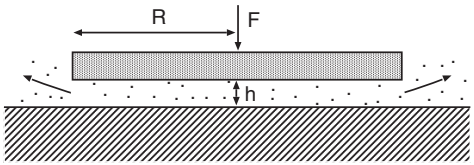


**Figure 5.** A rigid solid plate squeezed against a rigid flat substrate in a liquid.

important case is the squeezing of a rigid circular sheet against a flat substrate; see figure 5. In this case the thickness of the liquid layer at time $t$ is determined by

$$\frac{1}{h^2(t)} - \frac{1}{h^2(0)} = \frac{4t\sigma_0}{3\mu R^2}, \tag{4}$$

where $\sigma_0 = F/\pi R^2$ is the squeezing pressure. Note that for $h(t) \ll h(0)$, $h(t) \sim t^{-1/2}$. The pressure distribution in the liquid film is

$$P = P_{\text{ext}} - \frac{3\mu\dot{h}}{h^3}(R^2 - r^2) \tag{5}$$

where $\dot{h} = \mathrm{d}h/\mathrm{d}t$ is the velocity of the plate relative to the substrate, and $P_{\text{ext}}$ is the external pressure. Note that during squeezing $\dot{h} < 0$, so that $P > P_{\text{ext}}$ for $r < R$, i.e., the pressure in the film between the two solids is higher than the surrounding pressure. During separation, $\dot{h} > 0$ and the pressure in the liquid film is below the pressure in the surrounding, which may lead to cavitation.

### *3.2. Elastohydrodynamics*

Real solids are never perfectly rigid as assumed above. Thus, when two solids are squeezed together in a liquid, the pressure distribution which develops in the liquid will deform the solids elastically (or plastically, if the pressure is high enough). The elastic deformation of the solid walls will in turn change the flow field in the fluid. Thus to obtain the elastic deformation of the solid walls and the flow field in the fluid one must simultaneously solve the Navier–Stokes equations of hydrodynamics and the equations of continuum elastic mechanics. In addition, when the local pressure becomes high enough, as is usually the case for hard solids, e.g., in the context of ball bearings and gears, it is necessary to take into account the pressure dependence of the viscosity, which is usually well approximated by an exponential form $\mu = \mu_0 \exp(\alpha P)$. This is a very complex problem and very few analytical solutions are known. However, using dimensional arguments one can show that for solid walls with quadratic surface profiles the solution to the *elastohydrodynamic* problem described above depends only on two dimensionless parameters $g_1$ and $g_2$ [1, 56]. Thus, numerical solutions of contact problems involving spherical and cylindrical geometries have been presented and fitted to simple analytical expressions involving the parameters $g_1$ and $g_2$.

In this section we present a simple qualitative argument to illustrate how the pressure distribution in the liquid deforms the solid walls. We focus on an elastically soft spherical object (e.g., a rubber ball) squeezed against a flat hard substrate in a Newtonian fluid. Since the ball is elastically soft, the pressure in the fluid will be so small that we can neglect the pressure dependence of the viscosity.

Consider first the problem of the elastic ball squeezed against the substrate *without* the liquid. In this case the ball will deform and a small circular contact area (radius $R$; see

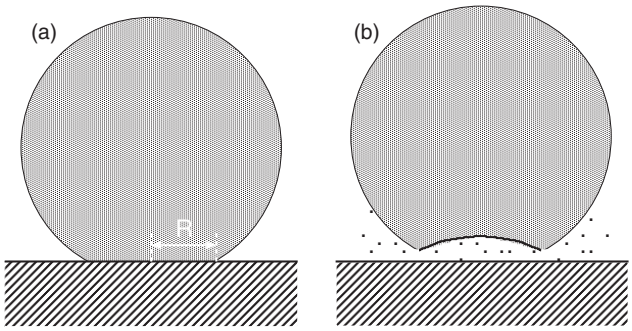


**Figure 6.** (a) Deformation of an elastic sphere squeezed against a flat hard solid in vacuum. (b) Deformation (snapshot picture) of the elastic sphere squeezed against the flat in a fluid.

figure 6(a)) is formed where the pressure distribution is given by the famous Hertz solution:

$$P_{\mathrm{H}} = P_0 \frac{3}{2}\left[1 - \left(\frac{r}{R}\right)^2\right]^{1/2} \tag{6}$$

where $r$ is the distance from the centre of the circular contact area. Now, consider pushing together the sphere and the flat in a fluid. We know that the pressure distribution $P_{\mathrm{H}}(r)$ will lead to locally flat surface. If a fluid layer is squeezed between two flat solid surfaces the pressure distribution is given by (5), i.e.,

$$P = 2P_0\left[1 - \left(\frac{r}{R}\right)^2\right]. \tag{7}$$

This pressure is larger (by a factor of $4/3$) in the centre of the contact area than that which would result in a locally flat surface. Thus, the elastic sphere tends to deform as indicated in figure 6(b).

### *3.3. Experimental results*

Here we present two sets of experimental results for elastohydrodynamic squeeze-out. We consider first liquids between soft solids (rubber), and then a case of intermediate substrate stiffness involving thin mica sheets. In both cases the pressure developed in the contact region is so small that the pressure dependence of the fluid viscosity can be neglected.

*Soft solids: rubber.* In a series of pioneering studies, Roberts and Tabor [57, 58] studied the squeezing of liquid films between rubber balls and flat hard substrates. The thickness of the liquid layer was deduced by studying the optical interference pattern from the junction.

As expected from the discussion in section 3.2, during squeezing of the rubber ball against the substrate in a liquid, the profile of the rubber surface in the contact zone bends upward, and the rubber–substrate separation is smallest at the periphery of the contact area; see figure 7. When the thickness of the film is below 400 Å, the surfaces suddenly spring together at various points leading to adhesive contact over a major part of the contact region. The contact first occurs at some protrusion (defects) near an edge of the contact zone where the film thickness is smallest; once a point of contact is established, this pulls the rest of the rubber into contact. This *dewetting transition* will be studied in detail in section 4.7.

With a low viscosity fluid such as water as the lubricant, at the stage of film collapse, surfaces seal together exceedingly quickly and trap small islands of water as shown in figure 8

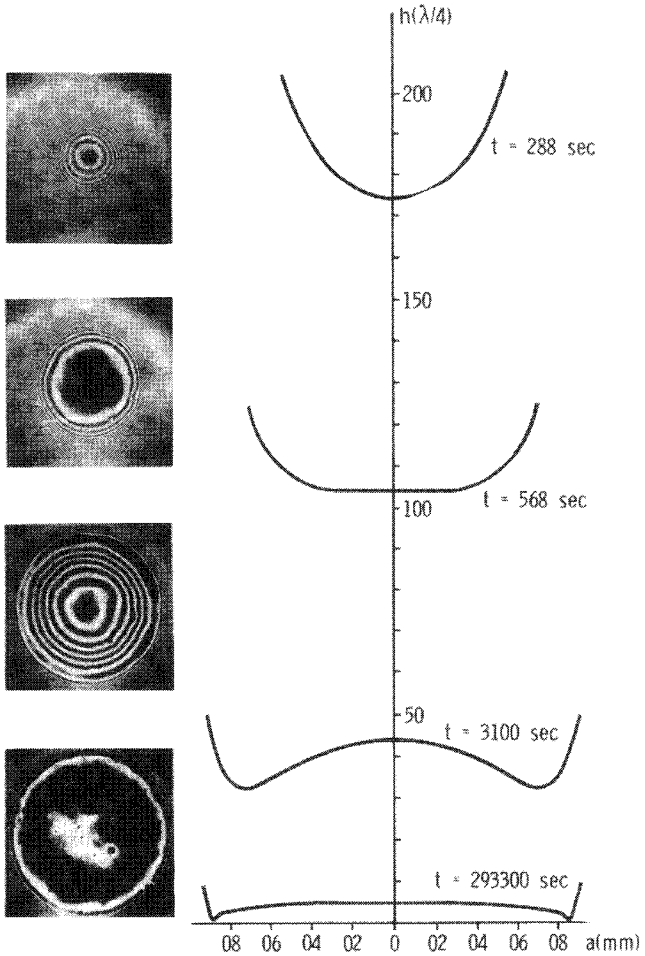


**Figure 7.** Left: interferograms produced as a spherical rubber ball comes into contact with a lubricated glass plate. The surfaces approach under constant load and squeeze out silicone oil. Right: thickness profiles which show the formation and collapse with time of a 'bell' entrapment of liquid ($\lambda = 4460$ Å). (From [58].)

(left). After a few hours these disappear, and Roberts suggested that this resulted from fluid flow in a thin ($\sim$15 Å) water layer at the interface. We do not believe that this is the correct explanation since if a water layer of this thickness were to occur at the interface the sliding friction would be extremely small. In contrast, the observed friction coefficient (at the sliding velocity 1 m s$^{-1}$) is $\mu \approx 8$, which is huge and nearly the same as for completely dry surfaces where $\mu \approx 10$. Thus, perhaps small water channels occur at the interface through which the fluid is squeezed out. A more likely explanation is a slow drift of the islands toward the periphery of the contact area, which results from the spatial (Hertzian) pressure distribution in the contact area; see section 4.4. If instead of distilled water a dilute solution of a negatively charged soap (sodium dodecyl sulphate (SDS)) is used, a drastically different result ensues; see figure 8 (right). The surfaces no longer spring together trapping islands of liquid, but instead remain apart at almost uniform separation of about 200 Å. The film does not collapse with time. In this case the film is stabilized by electrical double-layer repulsive forces which support

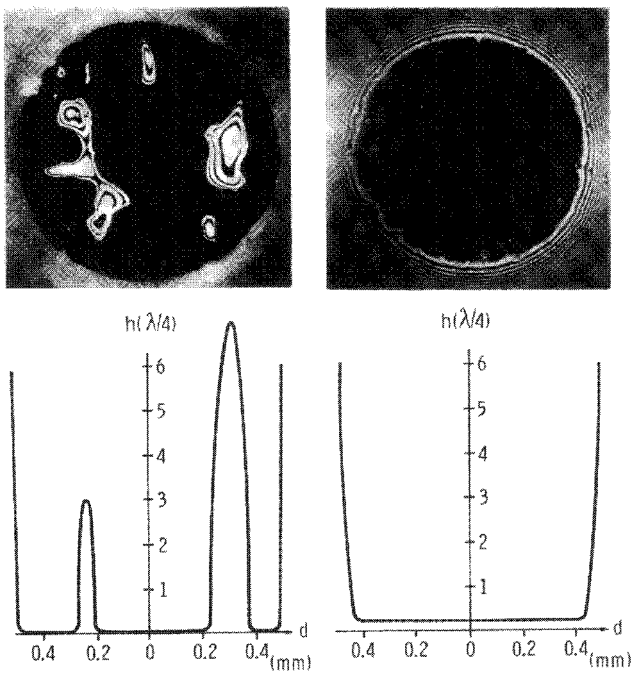


**Figure 8.** Interferograms (top) and deduced profiles (bottom) showing the marked difference between distilled water (left) and water containing 0.01 M SDS. Distilled water becomes trapped in pockets but the SDS solution forms a thin equilibrium film of about 200 Å uniform thickness. (From [58].)

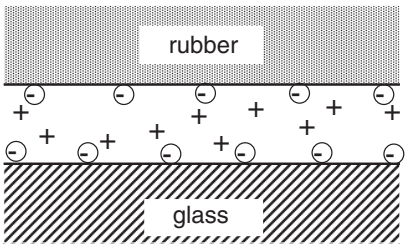


**Figure 9.** Water with positive ions (hydrated protons) between a rubber surface and a glass surface with negatively charged atomic groups. As the water with positive charges is gradually squeezed out the repulsive Coulomb force between the negatively charged solid surfaces will gradually increase.

the normal load, even when the squeezing pressure in the contact region equals ∼0.1 MPa. The SDS is absorbed on the rubber surface (see figure 9) with its negative polar end-groups in the water. The glass itself most probably acquires a negative charge by reaction between water molecules and the Si=O groups on the glass surface to form HOSi–$O^-$. The two negatively charged surfaces attract positive ions from the solution establishing a double layer of charge, resulting in repulsive forces between the surfaces at small wall–wall separation. One manifestation of this thin liquid layer is its lubrication effects: sliding at 1 m $s^{-1}$ results in a friction coefficient of ∼0.001 compared to ∼10 in dry conditions or in distilled water.

Roberts [58] also performed experiments in which positively charged soap was adsorbed on the rubber surface, the glass remaining negative. In this case the rubber and the glass surface

snap together (dewetting transition) and the friction is much higher. The possibility of affecting the adhesion and sliding friction of solids in liquids, by adsorbing molecules with ionic groups on solid walls, is of great practical use, e.g., for conditioner for hair-care applications (see section 4.12). The ability to modulate the contact between two soft solid bodies by changing the ionic composition of the surrounding fluid may also be very important in many biological processes, and we will give one example in sections 4.8 and 4.9.

*Intermediate substrate stiffness: thin mica sheets.* Whether a given surface behaves softly like the rubber ball described in the previous section, or more rigidly, depends on both the elasticity of the substrate material and on the speed used to squeeze the surfaces together. In SFA experiments, the effective elasticity of the substrates depends critically on the thickness $d$ of the intrinsically stiff mica sheets (typically $d \approx 1$–$3\ \mu$m) which reside on a soft glue layer (thickness: $\sim 10\ \mu$m or more). Figure 10 shows a series of video snapshots of the contact area in an SFA experiment with particularly thin mica sheets ($d \approx 400$ nm on both sides) [46]. The gap was filled with the model lubricant OMCTS. After equilibrating the surfaces at a separation of a few micrometres, they were pressed together rapidly by increasing the normal force abruptly. Within $\approx$100 ms the surface separation decreased to a few nanometres. Simultaneously, the elastic mica surfaces were flattened elastically and buckled inward slightly due to the hydrodynamic pressure (see also [11]). The cross section in figure 11 shows that the lubricant thickness was reduced to only one monolayer close to the perimeter of the contact area. This is the region where the lubricant layer ruptured in the following. Between the second and the fifth images in figure 10, a number of darker spots appear corresponding to direct mica–mica contact. As the collapse of the lubricant layer progresses, these areas grow and merge. Finally (last row), a finite amount of liquid is trapped inside the contact area. This nanodroplet shrinks laterally and becomes brighter, i.e. thicker, while conserving its volume. After a few seconds, it has transformed into a round droplet. (The fate of this droplet will be discussed below in section 4.4.) Qualitatively, the equilibrium shape of such nanodroplets is given by the balance of interfacial and elastic energies [44–46]. In contrast to the comparably thick trapped pockets discussed in the previous section, the nanodroplets still feel the presence of the oscillatory interface potential. Therefore, they assume a cylindrical shape with a flat top (figure 12).

## 4. Squeezing molecularly thin 2D liquid-like films

The basic theory of 2D squeeze-out was developed in [19]. Initially the system is trapped in a metastable state at the initial film thickness. Squeeze-out starts by a thermally activated nucleation process in which a density fluctuation forms a small hole, of critical radius $R_c \sim 10$ Å. Once it has formed, a 2D pressure difference $\Delta p$ develops between the boundary line separating the squeezed out region from the rest of the system, and the outer (roughly circular) boundary line of the contact area, thus driving out the rest of the 2D fluid.

### *4.1. Nucleation*

It has been shown both theoretically and experimentally that the layering transitions $n \rightarrow n-1$ start by a thermal fluctuation opening up a small 'hole' in the lubrication film as indicated in figure 13(a) for the $n = 1 \rightarrow 0$ transition. For a wetting liquid, e.g., hydrocarbons on metals or on metal oxides, the formation of a hole costs wall–lubricant binding energy and also line energy as a result of unsaturated bonds of the lubricant molecules toward the interior of the 'hole'. These (positive) energy terms scale as $\sim R^2$ and $\sim R$, respectively, with the radius $R$ of the hole. On the other hand, when the hole has been formed, the confining solid walls, which

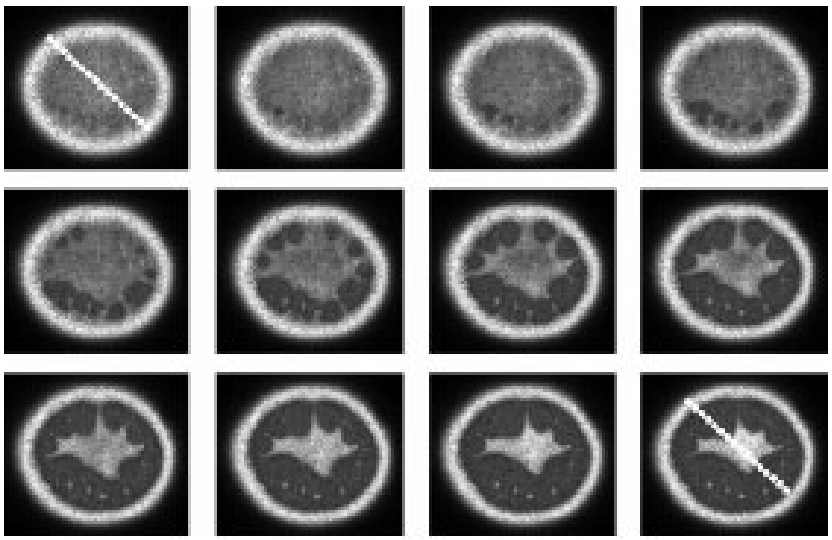

**Figure 10.** Video snapshots taken during a fast approach. (From left to right: $\Delta t = 150$ ms between images; image width $\approx$100 $\mu$m.) The bright ring marks the edge of the contact area. The intermediate grey level inside the contact area in the first image corresponds to a thickness of $\approx$1 nm. The darker grey level in the later pictures corresponds to direct mica–mica contact. The dashed lines in the first and last images indicate the directions of the cross sections in figures 11 and 12. (Adapted from [46].)

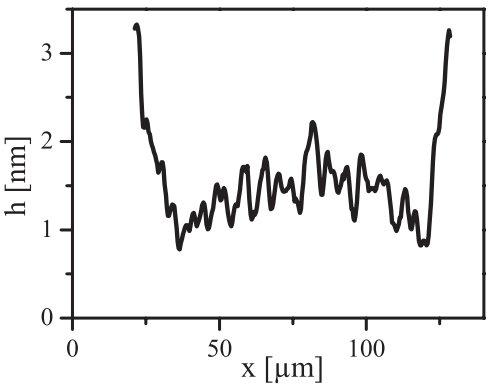


**Figure 11.** A cross section through the first image in figure 10 showing the elastohydrodynamic deformation of the mica substrates. (From [46].)

are squeezed together with a high pressure $P$, will relax inward at the hole as illustrated in figure 13(a). This gives rise to a (negative) relaxation energy which scales as $\sim R^3$ with the radius of the hole, so that the total free energy is of the form

$$U(R) = aR + bR^2 - cR^3, \tag{8}$$

where $a$, $b$ and $c$ are positive numbers, with $c \sim P^2/E$, where $E$ is the elastic modulus of the solid walls.

Let us prove that the elastic relaxation energy has the form given above. Before the hole is formed, the stress in the solid at the interface is $\sigma = P$, where $P$ is the squeezing pressure. When the hole has been formed, the stress is reduced to nearly zero in a volume element $\sim R^3$;

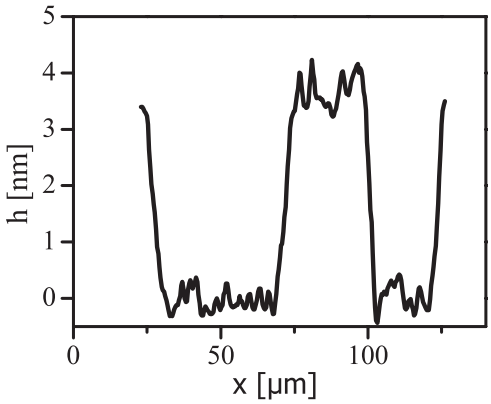


**Figure 12.** A cross section through the last image in figure 10. Note that the top of the droplet is flat, in contrast to the case for the much thicker droplets discussed in the previous section (figure 8). This reflects the range of the oscillatory layering forces. (From [46].)

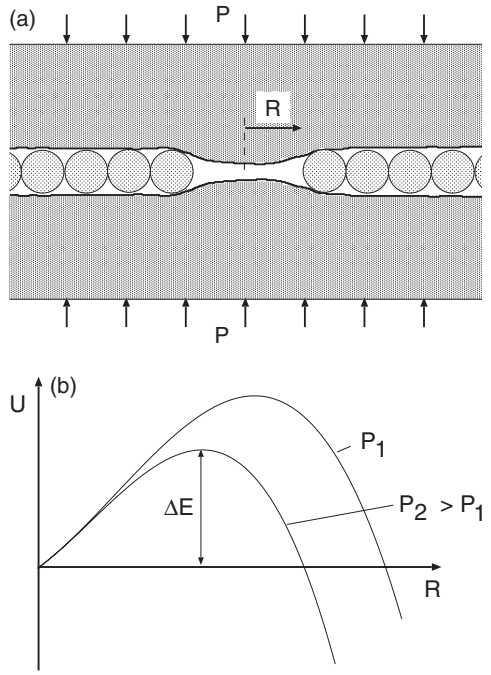


**Figure 13.** (a) The squeeze-out of the last lubricant monolayer from the contact area between two elastic solids. The squeeze-out is initiated by the formation of a small circular 'hole' (critical radius typically $R \approx 10$–$15$ Å). (b) The free energy $U(R)$ as a function of the radius $R$ of the hole. The barrier height $\Delta E$ decreases when the applied squeezing pressure $P$ increases.

see figure 14. Thus the change in the elastic energy is

$$\sim \int \mathrm{d}^3x\, \sigma\epsilon \approx \frac{1}{E}\int \mathrm{d}^3x\, \sigma^2 \approx \frac{P^2R^3}{E}, \tag{9}$$

where $\epsilon$ is the strain. This result is identical to the last term in (8).

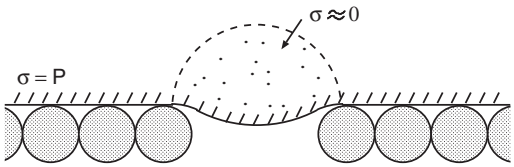


**Figure 14.** When a hole has been formed in the lubrication film, the solid wall relaxes inward resulting in a reduction in the elastic energy in the system. In the dotted volume element the stress in the solid is reduced from $P$ to nearly zero.

The function $U(R)$ has the form shown in figure 13(b). As the pressure $P$ increases the barrier $\Delta E$ decreases, and when the barrier becomes of order 1 eV the system can, due to a thermal fluctuation, 'jump' over the barrier in a macroscopic time period, say 1 s.

*Kinetics of film rupture.* Since the critical radius $R_c$ is too small, the nucleation stage cannot be tested using direct optical imaging. However, the value of the nucleation barrier can be inferred from measurements of the average force that is required to induce the squeeze-out as a function of the loading rate. Experiments of this kind were performed by Butt *et al* [23–25] using atomic force microscopy. These authors used substances consisting of hydrocarbon chains with a variety of polar head groups. These molecules form self-assembled monolayers or bilayers if deposited on polar substrates such as mica. Figure 15 shows a typical force versus distance curve. As the tip is pressed toward the surface, the film resists a finite load until it yields at some critical force. The mean yield force decreases with decreasing load rate (see the inset of figure 15). This kind of trend is well known for rate dependent thermally activated processes. It can be understood on the basis of simple kinetic theory. The probability rate for a film to rupture at a given pressure $P$ depends on the probability for a thermal fluctuation large enough to overcome the barrier $\Delta E(P)$:

$$w = w_0 \mathrm{e}^{-\Delta E(P)/k_B T}, \tag{10}$$

where $w_0$ is rate at which the tip attempts to penetrate the film. If the pressure is increased at a lower rate, the system spends more time within any finite interval $P$ to $P + \Delta P$. Hence the probability of developing a sufficiently large thermal fluctuation for a given value of $P$ is higher and the film will rupture, on average, at a lower pressure. *Inter alia*, Butt *et al* [23–25] used this dependence to measure the coefficients $a$ and $b$ (cf equation (8)), which include the line tension and the spreading pressure $p_0$, respectively, for several systems.

### *4.2. Spreading*

*Experimental findings.* Once a hole of the critical size has been formed, it spreads quickly across the contact area. While investigations of the nucleation process using optical imaging techniques are impeded by the small size of the critical radius, spreading can be followed in detail. In figure 16 we show a series of experimental snapshots recorded during the squeeze-out of one monolayer of OMCTS ($n = 3 \rightarrow 2$), corresponding to $\Delta h = 0.95 \pm 0.1$ nm. In the first image, the contact area, which is slightly elliptical, displays an intermediate grey level, corresponding to a film thickness of $n = 3$. In the second image, a brighter area with $n = 2$ appears close to the centre of the contact area. This $n = 2$ area spreads across the contact area within a few seconds. While it is approximately circular initially, it deforms progressively as it approaches the edge of the contact area (second row). At this time, some sections of the boundary line assume a negative curvature (see the black arrows). In the late stage of the

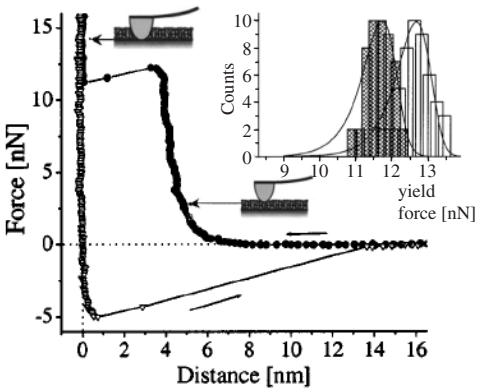


**Figure 15.** A typical force curve for a lipid bilayer (DOTAP) in aqueous solution. The inset shows yield force histograms for two different tip approach rates (0.8 $\mu$m s$^{-1}$ (left peak) and 5.6 $\mu$m s$^{-1}$ (right peak)). (Adapted from [23–25].)

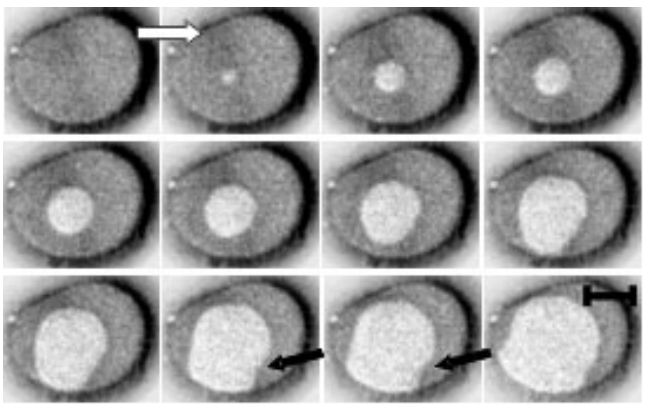

**Figure 16.** Experimental snapshots of the contact area during the $n = 3 \rightarrow 2$ layering transition (time between subsequent images: 0.1 s; scale bar: 25 $\mu$m). The initial grey level corresponds to a film thickness of $n = 3$ monolayers, and the brighter final one to $n = 2$. Black arrows point to segments of the boundary line with negative curvature formed close to the edge of the contact zone. The white arrow indicates the direction of time. (Adapted from [46].)

transition, the circular symmetry is completely broken. Similarly to the nucleation process described above, elastic relaxation of the mica substrates provides the driving force for the spreading of the $n - 1$ area. As a result a 2D pressure difference $\Delta p$ develops between the boundary line separating the squeezed out region from the rest of the system, and the edge of the contact area, thus driving out the rest of the 2D fluid, as illustrated in figure 17. This driving force is opposed by frictional dissipation, which is generated as the confined material slides past the solid substrates. In the following section, we describe the basic theory of squeeze-out of 2D liquid-like lubrication films. As we will see, the dynamics shown in figure 16 is reproduced by theory, which indicates that the lubricant is indeed in a two-dimensional liquid-like state.

*2D hydrodynamics: analytical results.* We focus on the evolution of the boundary line separating the $n$ and $n - 1$ regions during the layering transition $n \rightarrow n - 1$ for 2D liquid-like films, when the nucleation of the layering transition occurs in the centre of the contact

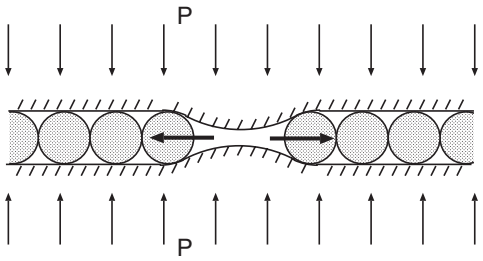


**Figure 17.** Because of the curvature of the solid walls at the boundary line, the perpendicular pressure $P$ will give rise to a parallel force component acting on the 2D lubrication film.

area. Since the lubrication film is assumed to be in a 2D liquid-like state, the basic equations of motion for the lubrication film are the continuity equation and the (generalized) Navier–Stokes equation for the 2D velocity field $\mathbf{v}(\mathbf{x}, t)$. Assuming an incompressible 2D fluid [1, 19],

$$\nabla \cdot \mathbf{v} = 0, \tag{11}$$

$$\frac{\partial \mathbf{v}}{\partial t} + \mathbf{v} \cdot \nabla \mathbf{v} = -\frac{1}{mn_a} \nabla p + \nu \nabla^2 \mathbf{v} - \bar{\eta} \mathbf{v}, \tag{12}$$

where $p$ is the 2D pressure, $\nu$ the 2D kinematic viscosity and $mn_a$ the mass density. The last term in (12) describes the 'drag force' from the solid walls acting on the fluid.

The contact area between the two solid surfaces is taken to have circular shape with radius $R$. Assume that the initial nucleation occurs at the centre of the contact. If we neglect boundary line instability effects (see section 4.3), then by symmetry the interfacial line between the squeezed and non-squeezed areas has a circular shape of radius $r(t)$. Let $p_1(r)$ be the 2D pressure at the (inner) moving boundary line and $p_0$ the spreading pressure at the (outer) boundary of the contact (at $r = R$). From the equations above one can show that [19]

$$\frac{\mathrm{d}A\,(t)}{\mathrm{d}t} \ln\left[\frac{A(t)}{A_0}\right] = -\frac{4\pi(p_1 - p_0)}{mn_a\bar{\eta}}, \tag{13}$$

where the squeezed out area $A(t) = \pi r^2$ and the total contact area is $A_0 = \pi R^2$. In [19, 22] we have shown that $p_1 = p_0 + P(r)a$, where $P(r)$ is the normal stress acting in the contact area (we assume radial symmetry) and $a$ is the width of the layer, typically of order 1 nm. If we assume constant normal stress $P_0$ then $p_1 = p_0 + P_0 a$ is position independent, and it is easy to integrate (13) to get [19]

$$\frac{A(t)}{A_0}\left(\ln\left[\frac{A(t)}{A_0}\right] - 1\right) = -\frac{t}{\tau}, \tag{14}$$

where $\tau$ is the time for complete squeeze-out:

$$\tau = \frac{mn_a\bar{\eta}A_0}{4\pi P_0 a}. \tag{15}$$

Under most normal circumstances, a Hertzian contact pressure distribution is a much better approximation, leading to squeeze dynamics in good agreement with experiments [21, 22]. The Hertzian pressure is

$$P(r) = \frac{3}{2}P_0\left(1 - \frac{r^2}{R^2}\right)^{1/2}. \tag{16}$$

Combining equations (13) and (16) we get [59]

$$\tilde{t} = \frac{4}{3}\left[\sqrt{1-\tilde{A}}(\ln\tilde{A} - 2) + \ln\left(\frac{1+\sqrt{1-\tilde{A}}}{1-\sqrt{1-\tilde{A}}}\right) + 2 - \ln 4\right] \tag{17}$$

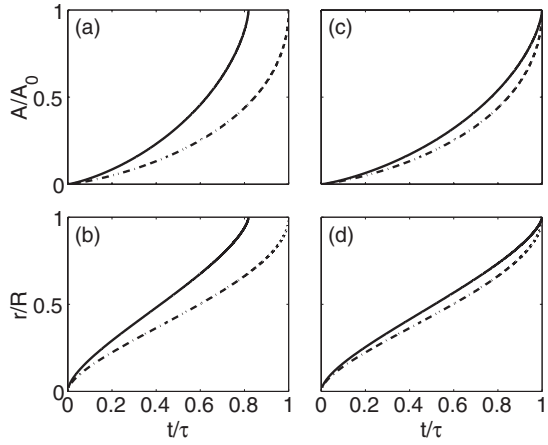


**Figure 18.** Analytical solutions to the centrosymmetric squeeze problem, for Hertzian normal stress (continuous curve) and a constant stress profile (dash–dotted curve). (a) Reduced area and (b) reduced radii ($r/R = (A/A_0)^{1/2}$) of the squeezed circle versus reduced time. (c) and (d) show the same as (a) and (b) but now with the Hertzian curves scaled such the total squeeze time is the same as in the constant stress case. (From [59].)

where $\tilde{A} = A/A_0$ and $\tilde{t} = t/\tau$.

Figure 18 shows the analytical solutions to the centrosymmetric case both for a Hertzian squeezing pressure (continuous curve, given by equation (17)) and for a constant pressure (dash–dotted curve, given by (14)). We show the variation of (a) the squeezed area and (b) the squeeze radii versus time. It is clearly seen that the Hertzian profile predicts faster squeeze-out (by roughly 20%), but qualitatively the two solutions are similar.

*2D hydrodynamics: computer simulations.* If the squeeze-out starts off-centre the symmetry properties assumed above are no longer valid, and one has to turn to numerical calculations. We have shown [21, 22] that the equations of motion can be transformed to a simpler form. Thus, using dimensional arguments, equation (12) can be simplified to

$$\nabla p + mn_a\bar{\eta}\mathbf{v} = 0. \tag{18}$$

This approximation assumes that the flow field is able rearrange itself much faster than the interfacial line motion. From (18) it follows that

$$\mathbf{v} = \nabla\phi, \tag{19}$$

where

$$\phi = -p/mn_a\bar{\eta}. \tag{20}$$

The continuity equation (11) then gives

$$\nabla^2\phi = 0, \tag{21}$$

which is a convenient starting point for numerical treatment.

We have performed kinetic Monte Carlo computer simulations of the squeeze-out process using the equations above (see [22]). In the simulations we also include a line energy $\Gamma$ between the squeezed out region and the 2D fluid region, chosen high enough to remove line boundary instabilities. The physical origin of this line energy is discussed in section 4.3. Its value is related to the effective elasticity of the mica substrates.

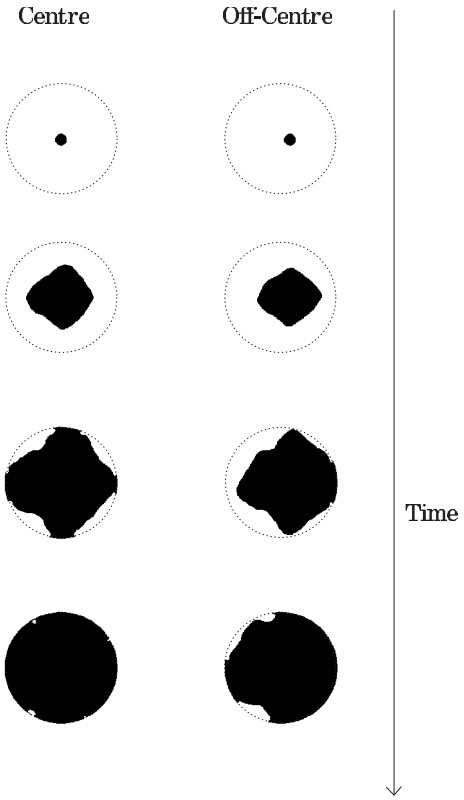


**Figure 19.** Simulation snapshots of squeeze dynamics. An initial (small) squeezed circular zone is assumed located in the centre of the contact (left figures) and slightly off-centre ($r = 0.15R$, right figures). The black area indicates squeezed zones and the white, fluid. The overall shape of the contact area is circular. A time arrow is also indicated. (From [59].)

We consider squeeze-out for the case where $\Gamma$ is so large that the 2D liquid boundary line is relatively smooth on the length scale of the contact area. We consider the cases where the nucleation starts in the centre of the contact area, and where it starts slightly off-centre ($r = 0.15R$). Figure 19 shows snapshots of the two systems. Note that the boundary line in the off-centre case propagates faster toward the nearest edge of the contact area, while the centred case evolves in a quasi-symmetrical fashion.

Figure 20 shows the time evolution of the effective radius $r/R = (A/A_0)^{1/2}$ of the squeezed area. We show both simulation results and the analytical result (from figure 18(d)). The agreement between the analytical formula and the simulations is excellent; the results differ only toward the end of the squeeze-out process, where the radial symmetry is completely lost. More remarkable is the agreement between the off-centre simulations and the analytical solution which is centrosymmetric. Figure 20 shows that the relation between the effective radius $r/R$ and the squeeze time $\tau$ is rather insensitive both to where the squeeze-out nucleates and to the detailed form of the squeezed out area. Note also that some sections of the boundary line assume a negative curvature (see figure 19) in the late stages of the simulations, in accordance with the experimental results shown above (figure 16).

In figure 20, we also show the effective radius $r(t)/R$ of the $(n-1)$ island, as determined from the experimental data shown in figure 16 (symbols). Obviously, the agreement between

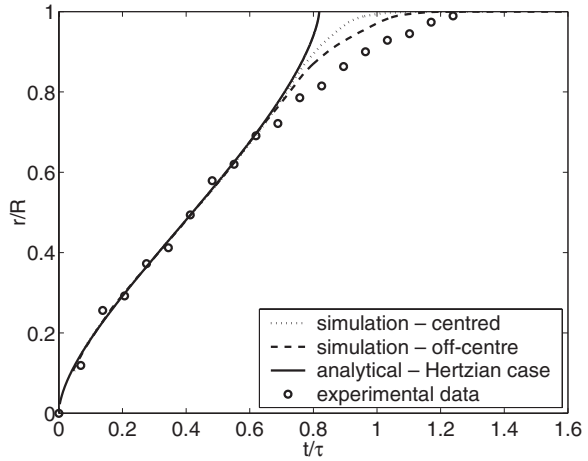


**Figure 20.** Effective squeeze radii from experiments simulations and analytical calculations. All calculations used Hertz stress profile. (From [59].)

the experimental data and both the analytical theory and the simulations are very good for $r(t)/R < 0.7$. The only adjustable parameter in this plot is the effective friction coefficient $\bar{\eta}$. For later times, the experimental data increase much more slowly than the analytical solution. This is not surprising since the circular symmetry is broken at this stage. The numerical results for off-centre nucleation, however, nicely reproduce the tail in the experimental data for long times.

### *4.3. Boundary line instability*

*Experimental results.* If the substrates are softer than in the experiments described above, the squeeze-out dynamics becomes more complex. Figure 22 shows another series of snapshot images recorded during a layering transition. The specific system investigated here was 1-undecanol ($C_{11}H_{23}OH$). This material forms self-assembled monolayers on mica with the OH groups pointing toward the mica surface [60]. On top of this effectively $CH_3$-terminated substrate any additional material inside the gap can slide very easily [61]. The entity that is expelled in figure 22 corresponds to a bilayer of $C_{11}H_{23}OH$, as sketched in figure 21. The total thickness of the two mica sheets together was less than 0.5 $\mu$m, making the solid walls effectively very soft. In these experiments, the bending of the boundary line (image 4 in figure 22) was much more pronounced than in figure 16. Furthermore, the boundary line became progressively rougher with increasing time. Ultimately, the roughness became so large that nanodroplets of liquid were detached from the overall dynamics and remained trapped inside the contact area in the final state. When the experiment was repeated approximately 100 times it turned out that nanodroplets were found at random locations. This proved that trapping was not caused by contamination at certain positions on the surfaces. There was a clear random character intrinsic to both the roughening of the boundary line and to the positions of the trapped nanodroplets.

*Theoretical description.* We will now show that the model presented in section 4.2 predicts rough boundary lines when the line energy $\Gamma$ is small. When $\Gamma = 0$, any small perturbation of the boundary line will be amplified, so that the boundary line is unstable with respect to

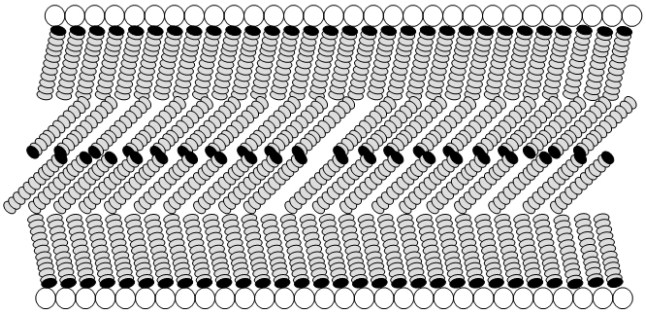

**Figure 21.** Surface bound $C_{11}H_{23}OH$ monolayers and an additional bilayer.

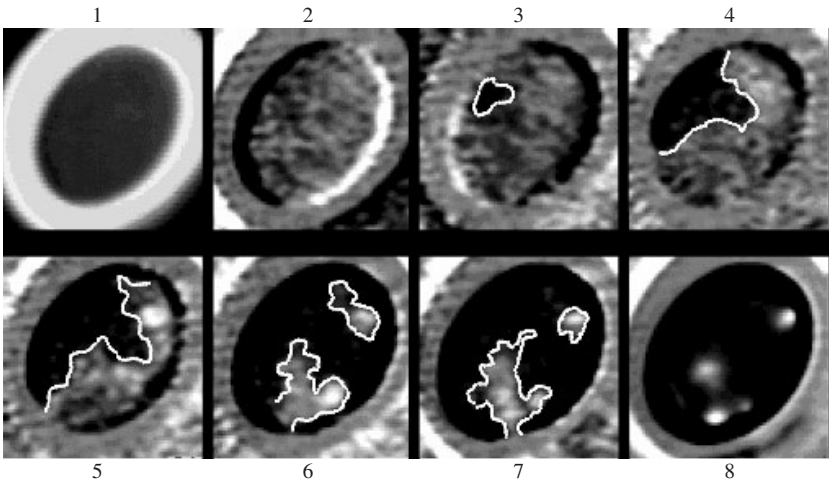


**Figure 22.** Snapshots of the contact area during the layering transition. Due to a different choice of the wavelength of light to that for figure 16, darker areas correspond to smaller film thickness in this case. Image 1 was subtracted from the original images 2–8 in order to improve the contrast. Images 2–7 were recorded at 0.16 s time intervals. (Adapted from [44].)

arbitrary small perturbations. In real systems such perturbations always exist, e.g., due to defects or thermal fluctuations.

It is easy to show that when $\Gamma = 0$, the time evolution of the boundary line is unstable with respect to small perturbations. Let us first consider a perfectly smooth circular boundary line centred at the centre of the contact area. For a perfect system (no defects or fluctuations), by symmetry such a boundary line would propagate in a symmetric (circular) way until it reached the outer boundary of the contact area. Now assume that, due to a fluctuation, a small protrusion is formed on the boundary line, which will locally decrease the distance to the outer boundary line $r = R$; see figure 23(b). By analogy to electrostatics, this will give rise to an enhanced 'draining' velocity of the fluid at the protrusion, so that the boundary line at the protrusion will move faster toward the periphery than in the other regions. This argument is valid for protrusions of any size, and it follows that, within the model discussed above, the boundary line will be *rough at all length scales*. This instability of moving boundaries is known in a slightly different context as Saffmann–Taylor instability. However, when the free energy (per unit length) $\Gamma$ (line tension) of the boundary line is taken into account, the

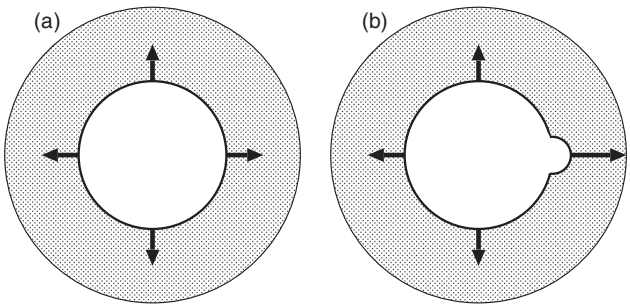


**Figure 23.** (a) Squeeze-out in the case of perfect symmetry. The boundary line is a circle. (b) When a small protrusion occurs on the otherwise circular boundary line, the squeeze-out velocity is enhanced at the top of the protrusion.

boundary line will be smooth on all length scales below some critical cut-off length $\lambda_c$, while it will be rough on longer length scales. It turns out that [20]

$$\lambda_c = 2\pi(\Gamma/mn_a\bar{\eta}v_0)^{1/2}, \tag{22}$$

where $v_0$ is the velocity of the boundary line.

The line tension $\Gamma$ has a contribution from unsaturated bonds at the boundary line, and another much larger contribution from the energy stored in the elastic deformation field in the confining solids in the vicinity of the boundary line. If $a$ denotes the difference in separation between the solid walls in the $n = 1$ and 0 regions (which is of order the thickness of a lubrication monolayer), then it follows from dimensional arguments that the elastic deformation energy per unit length of boundary line must be of order $Ea^2$. A more detailed argument is as follows: the elastic energy stored in the boundary line is

$$\sim\tfrac{1}{2}E\int \mathrm{d}^3x\,\varepsilon^2.$$

Now, the strain $\varepsilon \sim a/l$, where $l$ is the lateral distance over which the elastic displacement field varies along the solid surfaces perpendicular to the boundary line. Since the elastic displacement field satisfies a Laplacian-type equation in solids, it follows that $l$ is also the characteristic distance over which the displacement field extend into the solids. Thus the volume which contributes to the integral above will be of order $2\pi Rl^2$ (where $2\pi R$ is the length of the boundary line). Hence we get the line energy $\sim E(2\pi Rl^2)(a/l)^2 = (2\pi R)(Ea^2)$ so that $\Gamma \approx Ea^2$. In fact, an exact calculation (within the elastic continuum model) gives $\Gamma = Ea^2/2\pi(1-\nu^2)$.

The width $l$ depends on the applied perpendicular pressure and in some of the experiments $l$ may be larger than the thickness $d$ of the mica sheets. In this latter case the line energy will be smaller than given by the expression derived above, which is based on the assumption of a semi-infinite solid. To show this, assume that $l \gg d$ so that we can treat the mica sheets using the theory of elastic plates. Let $u(\mathbf{x})$ denote the vertical displacement field of a thin plate which originally (in the undeformed state) lay in the $xy$ plane. The elastic energy stored in the plate is given by [62]

$$E_{\text{plate}} = \frac{Ed^3}{24(1-\nu^2)}\int \mathrm{d}^2x\,[(\nabla^2 u)^2 - 2(1-\nu)|u_{ij}|],$$

where the determinant

$$|u_{ij}| = \frac{\partial^2 u}{\partial x^2}\frac{\partial^2 u}{\partial y^2} - \left(\frac{\partial^2 u}{\partial x\partial y}\right)^2.$$

Now, consider a bending deformation of the plate in the $x$-direction over an area of width (in the $x$-direction) $l$ and length (in the $y$-direction) $B$ with the displacement $a$. In this case $\nabla^2 u \sim a/l^2$ and similarly for $|u_{ij}|$ so that

$$E_{\text{plate}} \approx Ed^3 Bla^2/l^4 = Ed^3 Ba^2/l^3$$

so that $\Gamma \approx Ea^2(d/l)^3$. A more accurate calculation gives $\Gamma = 2Ea^2(d/l)^3/(1-\nu^2)$. If we neglect the elastic energy stored in the relatively soft glue layer used to attach the mica surfaces to the glass cylinders in the SFA, then we can write an interpolation formula for the line energy:

$$\Gamma \approx \frac{Ea^2}{2\pi(1-\nu^2)} \frac{1}{1+(l/d)^3/4\pi}. \tag{23}$$

From the discussion above it follows that the line energy $\Gamma$ can be varied by changing the thickness of the mica sheets. Thus, the line energy $\Gamma$ was exceptionally low in [44] (see figure 22), because the mica thickness was <500 nm, whereas it was 2.5 $\mu$m in the experiments reported on in section 4.2. For the simulation results presented below, we chose the line tension $\Gamma$ such as to reproduce the observed roughness of the boundary lines [22].

Under the experimental conditions in [44] equation (8) predicts $\lambda_c \sim 5$ $\mu$m, which equals 1/10 of the diameter of the contact area. The experimental boundary line for $C_{11}H_{23}OH$ is indeed rough at this length scale, while it is smooth on shorter length scales. On the basis of this result one may also argue that the linear size of the trapped islands should be of order $\lambda_c$ (or larger), which again agrees with the observations (see the bottom row of figure 22).

*Computer simulations.* We now present results of computer simulations of the layering transition, for the case where $\Gamma$ is so small that the boundary line is rough on a length scale much smaller than the diameter of the contact area. Figure 24 (top) shows snapshot pictures of the layering transition for a Hertzian contact pressure and with the line tension $\Gamma > 0$ chosen so that the boundary line is smooth on length scales smaller than about $R/10$, where $R$ is the radius of the contact area. Note that the boundary line is rough for all length scales (fractal) above a lower cut-off length $\lambda_c$ determined by the line tension. Figure 24 (bottom) shows snapshot pictures of the layering transition when the line tension $\Gamma = 0$. In this case a fractal pattern occurs for all length scales above the short distance cut-off length, given by the mesh size. This behaviour is in sharp contrast with experiment (figure 22) [44, 46, 59], showing the fundamental importance of the line tension $\Gamma$ for a correct description of the dynamics of the squeeze-out process.

During squeeze-out (figure 24 (top)) the local curvature of the boundary line between the $n = 1$ and 0 regions becomes strongly negative in some areas. As in the experiments, some of these areas eventually detach from the boundary and leave behind pockets of $n = 1$ layer trapped material in the final $n = 0$ state. The behaviour of these islands will be discussed in detail in section 4.4.

Figure 25 shows the same as figure 24, but now with a constant contact pressure, $P(r) \equiv P_0$. Note that the fast propagation along the periphery of the contact area causes trapping of a huge fluid island. When a Hertzian contact pressure is assumed, the increase in the squeeze-out speed close to the periphery is much smaller (since $P \to 0$ as $r \to R$), which makes it possible to squeeze out much more fluid from the interior of the contact area, resulting in much smaller 'trapped' islands, in qualitative agreement with experiment. We also note that in figure 25 the squeeze-out process stops when the drained area encircles the trapped island. At this point there is no pressure difference across the fluid and the dynamics stops. This is in sharp contrast to the Hertzian contact pressure case and to the experiments, where a squeeze-out force acts radially on any island of 'trapped' fluid.

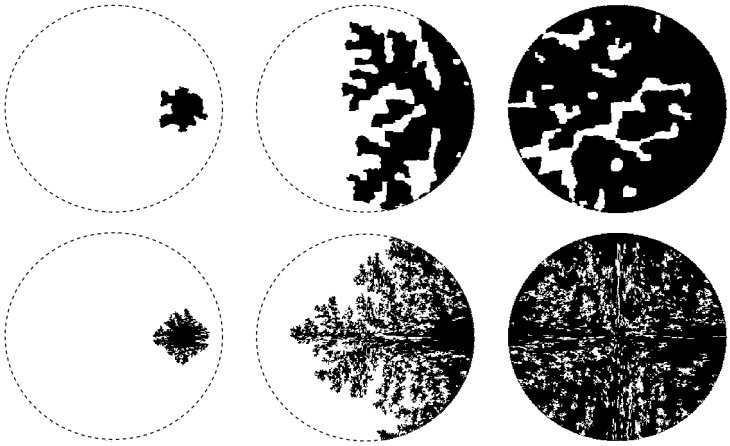

**Figure 24.** Snapshots of the layering transition for Hertz contact pressure with the line tension included (top), and with zero line tension (bottom). (From [21].)

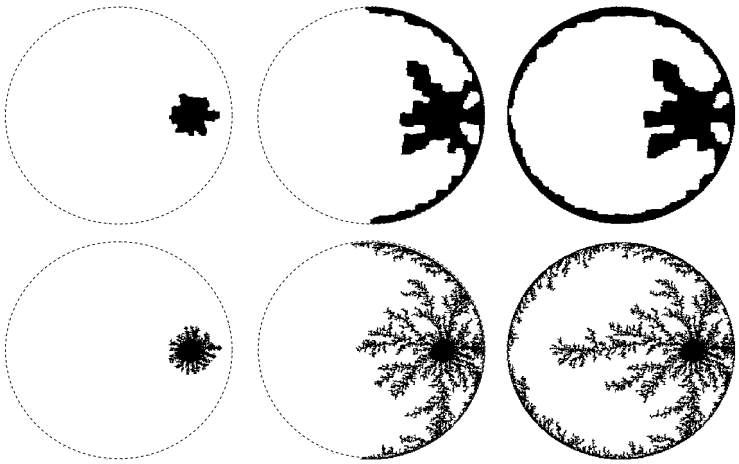

**Figure 25.** Snapshots of the layering transition for constant contact pressure with the line tension included (top), and with zero line tension (bottom). (From [21].)

### *4.4. Motion of trapped island*

*Experimental results.* Lubricant nanodroplets trapped inside the contact area are in general not stable. Due to the spatial variation in the normal stress from a maximum in the centre to zero at the periphery of the contact area, they experience a net force. Figure 26 shows the evolution of the droplet already shown in figure 10. The volume and shape of the droplet are essentially conserved while it drifts slowly from its original position toward the edge of the contact area. A careful inspection of the video data shows that the droplet motion in not perfectly homogeneous and continuous. Occasionally, the boundary line seems to get pinned locally before it continues to move. (Video clips can be viewed at www.wetting.de/sfa.htm.) The droplets accelerate as they approach the edge of the contact area. Ultimately, they become elongated along the radial direction and form small necks connecting them to the surrounding reservoir (bottom row of figure 26). Subsequently, most of the liquid is squeezed out through

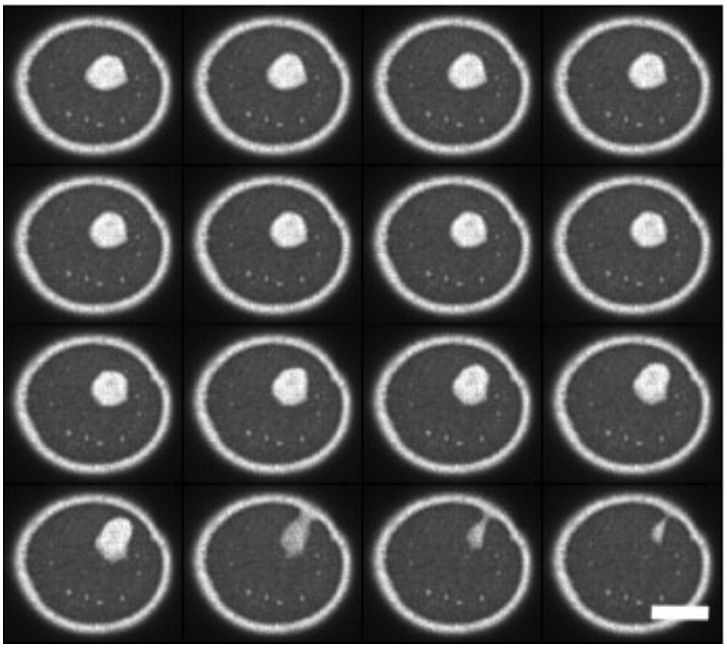

**Figure 26.** Snapshots during squeeze-out of a nanodroplet with $n = 4$. (Scale bar: 20 $\mu$m; $\Delta t = 0.5$ s between images.)

these necks. It is remarkable, however, that a finite amount of liquid usually remains trapped inside the contact area even in the final state. The same was observed for the nanodroplets shown in figure 22. In those experiments, the droplets did not move at all once they were formed [44], but remained trapped inside the contact area indefinitely.

*Hydrodynamic description.* The analysis of the dynamics is straightforward. The elastic energy stored in the solids at a trapped island can be written as

$$U = \int \mathrm{d}^2x \; P(\mathbf{x})h(\mathbf{x}), \tag{24}$$

where $P(\mathbf{x})$ is the 3D squeezing pressure. When the squeezing pressure is constant, $P(\mathbf{x}) \equiv P_0$, we get

$$U = P_0 \Delta V$$

where $\Delta V$ is the volume of the trapped island. Thus, in this case the elastic energy is independent of the location of the island in the contact area. This implies that the external squeezing pressure will not exert any tangential force on the island. However, when $P(\mathbf{x})$ varies with the location $\mathbf{x}$ in the contact area, the energy $U$ will also depend on the location of the island, which will give rise to a tangential force on the island. If we assume that the shape of the island does not change when we vary the (centre of mass) position $\mathbf{r}$ of the island, and if we assume that the island is disc-like with thickness $h_0$, then

$$\frac{\partial h}{\partial \mathbf{r}} = h_0 \oint \mathrm{d}s \; \mathbf{n}_s \delta[\mathbf{x}_s - (\mathbf{x} - \mathbf{r})],$$

where the line integral is over the boundary of the island ($s$ is the boundary length coordinate), $\mathbf{x}_s$ is the position vector of the boundary line relative to the centre of mass position $\mathbf{r}$ of the

island and $\mathbf{n}_s$ is the local normal to the boundary line, pointing away from the island. Thus we get the force on the island

$$\mathbf{F} = -\frac{\partial U}{\partial \mathbf{r}} = -\oint \mathrm{d}s\, h_0 P(\mathbf{r} + \mathbf{x}_s)\mathbf{n}_s. \tag{25}$$

Using this formula, we find that the forces acting on the nanodroplets in the experiments are typically of the order of $10^{-8}$–$10^{-7}$ N. If we divide this by the droplet area, we obtain a typical shear stress of no more than 1 kPa.

For a small island the pressure $P$ will vary very little over the island and we can make the approximation

$$U = \int \mathrm{d}^2x\, P(\mathbf{x})h(\mathbf{x}) \approx P(\mathbf{r}) \int \mathrm{d}^2x\, h(\mathbf{x}) = P(\mathbf{r})\Delta V. \tag{26}$$

If we assume that $P(\mathbf{r})$ only depends on the distance $r = |\mathbf{r}|$ from the centre of the contact area, we get the radial acting force

$$F = -P'(r)\Delta V. \tag{27}$$

Let us consider the motion of a small (compared to the size of the contact area) island with height $h_0$ and area $\Delta A$, which we assume does not experience any pinning forces. We will calculate the dependence of the velocity $v(r)$ of the island on the distance $r$ from the centre of the contact area. We assume overdamped motion, and can thus neglect the inertia force acting on the island, so that the driving force $F(r)$ must just balance the frictional drag force from the solid walls:

$$n_\mathrm{a}\Delta A m\bar{\eta}v(r) = F$$

or

$$v = -\frac{h_0}{n_\mathrm{a} m\bar{\eta}}P'(r).$$

If $P(r)$ is given by the Hertz expression (7) then this gives

$$\frac{v}{v_0} = \frac{r}{R}\left(1 - \frac{r^2}{R^2}\right)^{-1/2}, \tag{28}$$

where

$$v_0 = \frac{3}{2}\frac{h_0 P_0}{n_\mathrm{a} R m\bar{\eta}}. \tag{29}$$

This function is shown in figure 27(a). Note that the velocity goes to infinity for $r = R$. However, for any finite size island (radius $b$), when $r = R - b$ the island will make contact with the region outside the contact area, and, as we saw above (figure 26), the liquid drop will be squeezed out through a small neck; this behaviour was reproduced in computer simulations.

It is easy to integrate (28) to get the radial position $r(t)$ of the island as a function of time. In particular, the time $t$ it takes to squeeze out an island is given by

$$\frac{t}{t_0} = \int_{r/R}^{1} \mathrm{d}x \left(\frac{1}{x^2} - 1\right)^{1/2} \tag{30}$$

where $r = r(0)$ is the initial distance of the island from the centre of the contact area, and $t_0 = R/v_0$. This function is shown in figure 27(b).

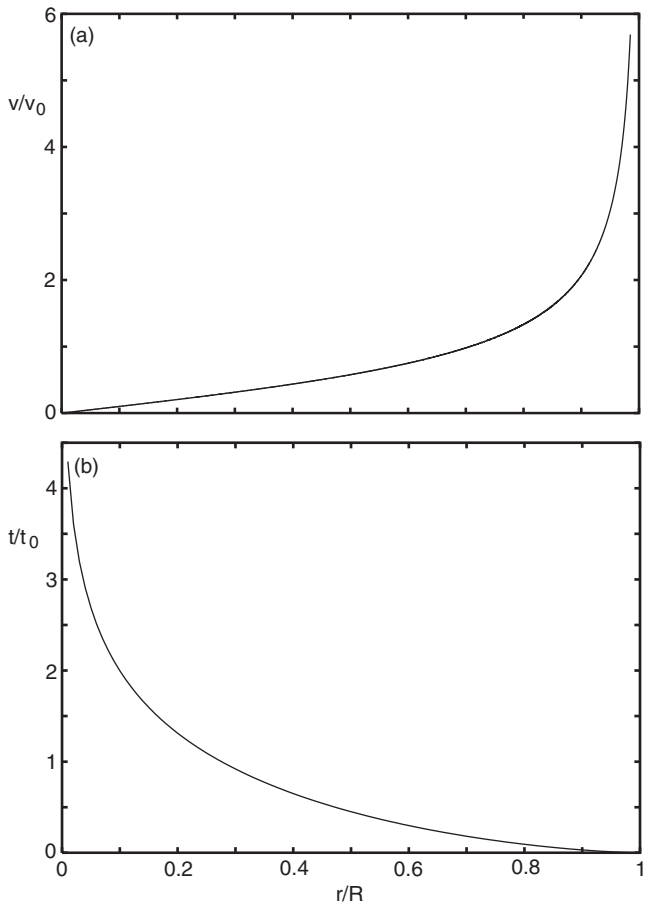


**Figure 27.** (a) The radial velocity $v$ of a small island as a function of the distance $r$ from the centre of the contact area. (b) The time $t$ it takes to squeeze out a small island as a function of the initial distance $r$ from the centre of the contact area.

*Pinning and numerical results.* From the experiments it is clear that the trapped islands withstand a finite shear stress in some cases. Clearly, a perfect fluid in a homogeneous surrounding is not expected to do so. Either the droplets are transformed into a solid-like state pinned by the atomic corrugation of the solid walls (which hence require a finite shear stress to depin), or the substrates are in fact not perfectly homogeneous. The former possibility is particularly attractive since it conforms with earlier reports on confinement induced solidification [17, 18]. However, the initial nanodroplet in figure 26 moved although the total shear stress acting on it was only $\approx$1 kPa. The critical shear stress of a potentially solidified film would thus be extremely low. Chemical heterogeneity due to adsorption of contamination seems to be more likely. Under typical experimental conditions, the applied pressure is of the order of 1 MPa and $h_0 \approx 1$ nm, corresponding to an elastic energy per unit area of 1 mJ m$^{-2}$. Any heterogeneity of the surface energy of that order would be sufficient to pin a droplet. Since $P$ decreases toward the edge of the contact area, even less heterogeneity is sufficient there. If pinning centres occur at the interface, they will cause fluctuations of the velocity $v(r)$ of the island, and in a distribution of squeeze-out times (for identical starting distance $r(0)$). Currently available experimental data support this idea qualitatively, but do not

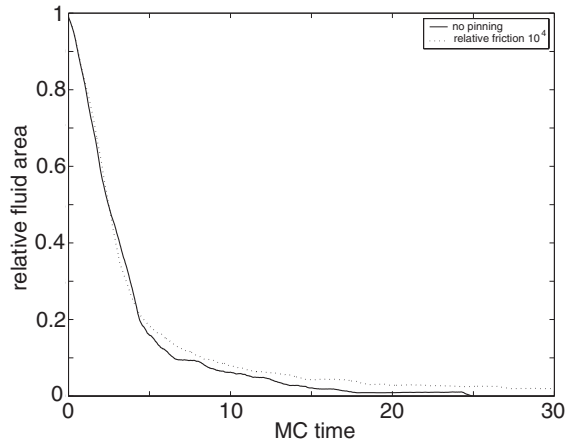


**Figure 28.** The fractional area occupied by the fluid as a function of time without (solid curve) and with (dotted curve) pinning centres, and with the squeeze-out nucleus at $r = 0.6R$.

allow a quantitative comparison. Nevertheless, detailed future studies of the motion of islands will give information about the nature of the pinning dynamics.

In recent numerical simulations, a different procedure was used to model pinning. Namely, we introduced small, high friction areas, where $\bar{\eta}$ was taken to be $10^4$ times higher than in the remaining area. This produced pinning of the fluid in these areas, resulting in a finite amount of trapped liquid even for very large times. Figure 28 shows the variation of the fractional area occupied by the fluid as a function of time without (solid curve) and with (dotted curve) pinning centres, assuming that the initial $n = 0$ nucleus occurs at $r = 0.6R$. Without pinning centres, the liquid is squeezed out completely. In the presence of pinning centres, however, about 1.3% of the liquid remains trapped at the interface for large times. The data were obtained from the kinetic Monte Carlo simulations discussed in the previous section [21]. The solid curve in figure 29 shows the same data, but this time for an initial position of the nucleus at $r = 0.7R$, and with a concentration of pinning areas, corresponding to about 13% of trapped fluid remaining for longer times. These parameters mimic the experimental conditions of figure 22. The circles are the experimental results.

Let us return to the experimental observation of Roberts of a very slow removal of water droplets trapped at the interface between a rubber ball and a glass substrate (section 3.3). Assume that the droplets drift slowly toward the periphery of the contact area because of the change in elastic energy with the lateral position of the droplet. We assume that the radius $r_0$ of the bottom surface of the droplet is small compared to the radius $R$ of the contact area, so that the lateral force is given by $F = -P'(r)\Delta V$. Assume first that the rubber–glass interface is perfect, e.g., without surface roughness and contamination. If we assume no-slip boundary conditions on the glass and rubber surfaces, then the viscous dissipation of energy per unit time inside the water droplet is of order

$$\mu\left(\frac{v}{H}\right)^2 \Delta V$$

where $H$ is the height of the droplet. Thus the speed of the squeeze-out is given by

$$-P'(r)v \approx \mu\left(\frac{v}{H}\right)^2$$

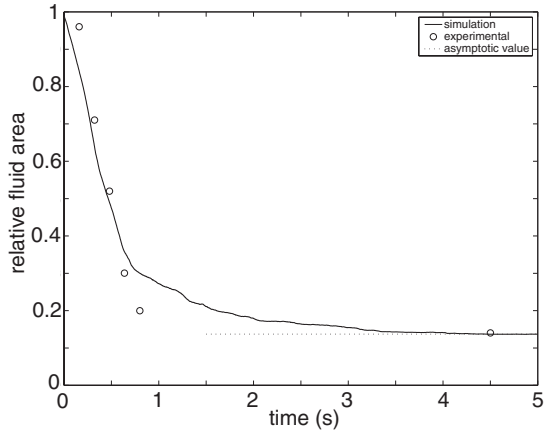


**Figure 29.** The fractional area occupied by the fluid as a function of time with the initial position of the squeeze nucleus at $r = 0.7R$. Solid curve: theory. Circles: experimental. (From [21].)

or

$$v \approx -P'(r)H^2/\mu.$$

Since $-P'(r)$ is of order $P_0/R$, we get

$$v \approx H^2 P_0/(\mu R)$$

and the squeeze-out time will be of order

$$\tau \approx \frac{R}{v} \approx \left(\frac{R}{H}\right)^2 \frac{\mu}{P_0}.$$

In a typical case $H \approx 10^{-6}$ m, $R \approx 10^{-3}$ m, $P_0 \approx 10^5$ Pa and (for water) $\eta \approx 10^{-3}$ N s m$^{-2}$ giving $\tau \approx 0.01$ s. However, the observed squeeze-out time was several hours. We believe that the explanation for this discrepancy is related to surface defects which give rise to pinning of the boundary line. Thus, the situation is probably very similar to the motion of a liquid droplet on a tilted flat glass substrate (where the gravitational force is the driving force), where contact angle hysteresis usually occurs as a result of pinning of the boundary line by surface defects. This manifests itself in an advancing contact angle $\theta_a$ (the front angle in the direction of droplet motion), which is larger than the receding angle $\theta_r$ (the rear contact angle). The pinning force per unit length of the boundary perimeter can be related to $\theta_a$ and $\theta_r$, and is typically of order $\gamma_p \approx 0.01$ N m$^{-1}$. The ratio between the driving force

$$F = -P'(r)\Delta V \approx P_0 \Delta V/R$$

and the pinning force

$$F_p \approx 2r_0\gamma_p$$

is of order

$$\frac{\pi}{2}\frac{P_0 H r_0}{\gamma_p R}.$$

Since typically $\gamma_p = 0.01$ N m$^{-1}$ and $r_0 \approx 10^{-4}$ m we get a ratio of order 1. Thus the driving force is of similar magnitude to the pinning force, and it is clear that if a droplet were to be pinned according to the argument presented above, it might still drift slowly due to thermally activated local depinning of (small) boundary line segments (creep motion). We believe that this is the origin of the water droplet squeeze-out in the Roberts experiments.

### *4.5. Role of the 2D lubricant compressibility*

So far we have assumed that the lubricant behaves as an *incompressible* 2D liquid. While that assumption is quite good for many practical situations, recent computer simulations [37] have shown that, at least at high squeezing pressures, strong density fluctuations may occur in the lubrication film. For example, in [37] it was found that during the layering transition $n = 2 \rightarrow 1$, while islands of (temporarily) trapped bilayer ($n = 2$) were removed by being squeezed into the monolayer, the density of the monolayer film was much higher in the region close to the trapped $n = 2$ islands than further away; see figure 30. This resulted in a 2D pressure gradient in the film which induced a flow of the lubricant molecules away from the trapped islands. This kind of situation clearly calls for a consideration of the finite compressibility of the film.

The squeezing of one layer into another layer, as in figure 30, has also been observed in experiments. Thus, in figure 31 we show the consecutive collapse of two liquid layers ($4 \rightarrow 3 \rightarrow 2$). Due to the high load rate, nucleation of the first collapse occurs at several locations simultaneously (top row), as in figure 10. The volume of the bright area in the top row decreases with time, because material is squeezed out from this area into the reservoir through the two other remaining layers. Since the images only depend on the separation between the surfaces at the interface, no information about in-plane density fluctuations can be inferred from the pictures. For the transition $3 \rightarrow 2$, there is only one nucleation site (cf image 7).

In [63] we have studied the dynamics of the expulsion of the last liquid monolayer of molecules confined between two surfaces by solving the two-dimensional (2D) Navier–Stokes equation for a *compressible* liquid monolayer. The influence of the compressibility on the squeeze-out is characterized by the parameter $g_0 \approx P_0/\rho c^2$, where $P_0$ is the average perpendicular (squeezing) pressure, $\rho$ the liquid (3D) density and $c$ the longitudinal sound velocity in the monolayer film. When $g_0 \ll 1$ the 2D liquid can be considered as incompressible, in which case the results of the earlier treatment (see section 4.2) are reproduced. The main changes due to compressibility occur right at the onset of the squeeze-out process, and just before its completion.

Using the typical values $\rho \approx 1000$ kg m$^{-3}$ and $c \approx 700$ m s$^{-1}$ we get $\rho c^2 \approx 0.5$ GPa. In the experiments described in sections 4.2–4.4 (as well as in most other surface force apparatus studies) the average squeezing pressure $P_0 \ll 0.5$ GPa which implies that the liquid can be considered as incompressible. Thus the use of the theory described in section 4.2 was indeed justified. However, in many practical situations the pressure $P_0$ might be similar to the yield stress of the solids which for metals is typically of order 1 GPa. In these cases it is necessary to include the finite compressibility of the lubricant in order to accurately describe the squeeze-out dynamics.

In [63] it was found that for a Hertzian squeezing pressure profile, $P(r) = P_{\mathrm{H}}(r)$, the squeeze-out time depends on the compressibility, increasing from $\approx 0.8183\tau$ to $1.3333\tau$ as the compressibility increases from $B = 0$ to $\infty$, where $\tau$ is the squeeze-out time for an incompressible 2D fluid with constant squeezing pressure (see section 4.2). In figure 32 we show the squeeze-out time as a function of $g_0$.

The main effect of compressibility appears at the beginning and at the end of the squeeze-out process. Initially, compressibility favours piling up of fluid at the boundary line between the squeezed out area and the 2D fluid, which can as a result expand more rapidly, compared with the case of an incompressible fluid. On the other hand, when the hole approaches the boundary of the contact region, the squeezing out speed of the compressed fluid is smaller, due to its increased 2D density and, consequently, friction. In the case of uniform 3D squeezing pressure, $P(r) \equiv P_0$, these two effects compensate exactly, leading to a total squeeze-out time

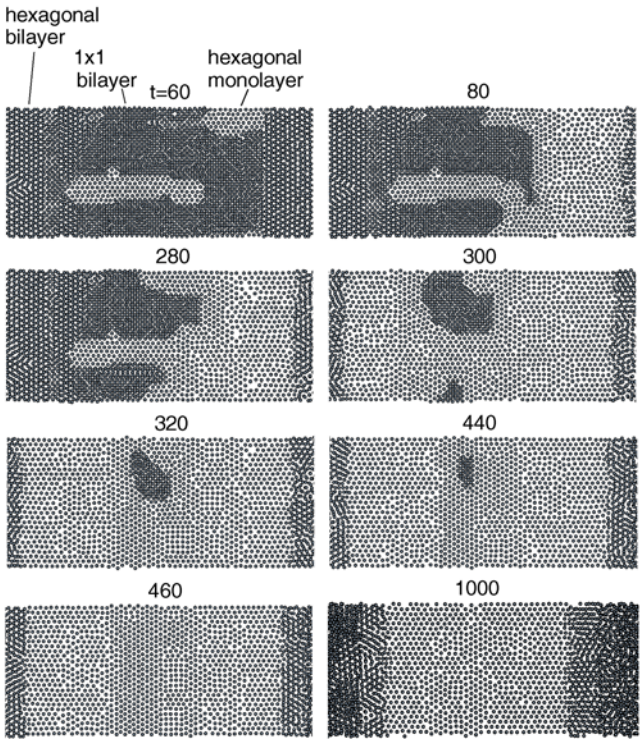


**Figure 30.** Squeeze-out of a monolayer (the $n = 2 \rightarrow 1$ transition) of Xe from the contact region between two curved steel surfaces (see section 4 for details of the model). These pictures show the central part of the contact area. The dark (fine grained) grey area is a (bilayer) $1 \times 1$ structure, while some hexagonal (bilayer) Xe structure can be observed at the periphery of the contact area in snapshot pictures $t = 60$, 80 and 280. The dotted area is the hexagonal Xe monolayer film which remains after the $n = 2 \rightarrow 1$ transition is completed. We note that even though most of the bilayer disappears in the two rapid transitions ($t = (60, 80)$ and $(280, 300)$) an island of $1 \times 1$ bilayer remains trapped for a while, and only gradually disappears as it is squeezed *into* the first monolayer. This process is accompanied by a lateral flow of atoms in the monolayer film toward the periphery of the contact area. The speed of the island squeeze-out is determined by the sliding friction as a patch of Xe monolayer film slides relative to the solid walls. Note that the local concentration of Xe atoms in the vicinity of the bilayer island is somewhat higher than far away; thus, there must be a 2D pressure gradient in the monolayer film which, of course, is the driving force of the lateral flow. During the flow this pressure gradient is mainly balanced by a frictional shear stress acting on the monolayer film as it slides or drifts relative to the solid walls.

independent of the compressibility. For a Hertzian pressure distribution, the squeeze-out time instead increases with increasing compressibility: the initial speed up is overcompensated by the enhanced friction at the periphery of the contact area.

### *4.6. Role of the perpendicular pressure*

In a very recent paper Mukhopadhyay *et al* [64] have used fluorescence correlation spectroscopy to study diffusion in molecularly thin confined layers of OMCTS. Spatially resolved measurements showed that translational diffusion slows exponentially with increasing perpendicular pressure from the edges of a Hertzian contact toward the centre, suggesting that friction reflects a disproportionate contribution from those more sluggish molecules that reside

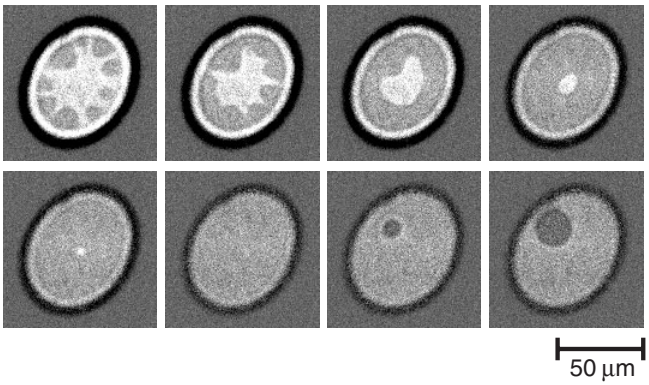


**Figure 31.** Consecutive collapses of two liquid layers ($4 \rightarrow 3 \rightarrow 2$). Due to the high load rate, nucleation of the first collapse occurs at several locations simultaneously (top row), as in figure 10. The volume of the bright area in the top row decreases with time, because material is squeezed out from this area into the reservoir through the two other remaining liquid layers. For the transition $3 \rightarrow 2$, there is only one nucleation site (cf image 7). (Total time: 1 s; image width: 80 $\mu$m; bright: thicker liquid layer; dark: thin.)

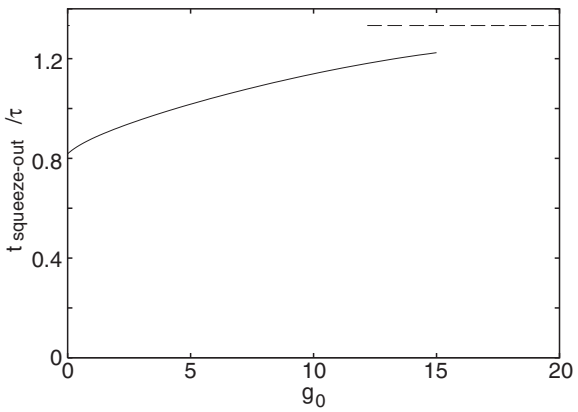


**Figure 32.** The dependence of the squeeze-out time on the compressibility parameter $g_0$ for a Hertzian squeezing pressure.

near the centre of a contact zone. On the basis of the Einstein relation, one may be tempted to assume that the sliding friction, $\bar{\eta}$, which enters in the squeeze-out dynamics, will have a similar pressure dependence to the (inverse of the) diffusivity. However, we have shown in [59] that this assumption leads to a squeeze-out dynamics in complete *disagreement* with the experiments [41, 44, 46].

Mukhopadhyay observed that the diffusivity in an OMCTS film, three monolayers thick, depended exponentially on the perpendicular pressure, $D \sim \exp[-\alpha P(r)]$, where $\alpha$ is an empirical exponent and $P(r)$ is the normal stress which we will take to be of the Hertzian form. In accordance with the Einstein relation we assume $\bar{\eta} \sim 1/D$ so that $\bar{\eta}(r) \sim \exp[\alpha P(r)]$. In figure 33 we show the dependence of the squeeze radius on time for different values of the parameter $\lambda = (3/2)\alpha P_0$, where $P_0$ is the average pressure in the contact zone. From the diffusion experiments in [64] we deduce $\lambda \approx 8.6$. Note that when $\lambda$ increases, the squeeze-out is slower at the early stages up to $r/R \approx 0.7$, after which it becomes significantly faster.

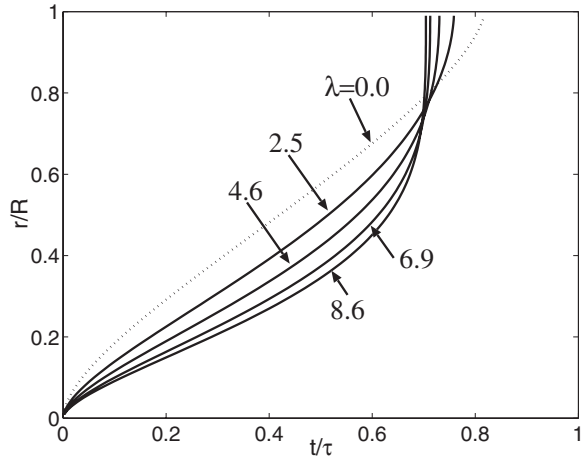


**Figure 33.** Squeeze radius versus time, for different values of λ. (From [59].)

However, the complete squeeze-out time is rather insensitive to the value of λ, and even for very large λ it is only ∼15% smaller than for $\lambda = 0$. The reduction in the squeeze-out time saturates as we increase λ.

It is clear that, if one assumes that the sliding friction is related to the diffusivity via the Einstein relation, the squeeze-out dynamics predicted with a position dependent friction is in complete *disagreement* with the diffusivity experiments of Mukhopadhyay *et al*. Our analytical results and computer simulations show that only a *very weak r* dependence of $\bar{\eta}$ is possible if one is to avoid disagreement with the measurements in figures 22 and 16 [41, 44, 46]. Perhaps this observation is related to a phase transformation of the lubrication film from a solid-like state before squeeze-out to a liquid-like state during squeeze-out. In any case the observed discrepancy seams to be very fundamental, and requires much more investigation.

### *4.7. Dewetting of soft interfaces*

In the discussion above, the squeeze-out of a liquid is due to an external applied squeezing force. However, for a nonwetting liquid between elastically soft solid walls, e.g., rubber, the squeeze-out can also result (even when the applied squeezing force vanishes) from the adhesive interaction between the solid walls. The dewetting of a liquid film intercalated between a solid substrate and a rubber surface is a topic of both great scientific interest and of practical importance, e.g., for wiper blades, or rubber friction on a wet substrate [57, 58]. Dewetting is also likely to be of great importance in many biological applications, e.g., involving cell adhesion to a substrate.

Consider a liquid squeezed between two smooth solid walls. Two limiting cases have been observed and studied for the squeeze-out dynamics (see figure 34). Thus, as shown above, for hard solid walls the squeeze-out of the last few monolayers of a wetting [46] or nonwetting [44] liquid occurs in a quantized manner, involving a monolayer at each step; see figure 34(a). The layering transition $n \rightarrow n-1$ (where $n$ is the number of trapped monolayers) typically nucleate in the central, high pressure region of the contact area, and spread circularly toward the periphery of the contact area. During the whole squeeze-out process, the surfaces are locally separated by either $n$ or $n-1$ monolayers, e.g., no rim of thicker fluid film is formed at the boundary line between the $n$ and $n-1$ thickness regions. Instead, the $n$-monolayer region

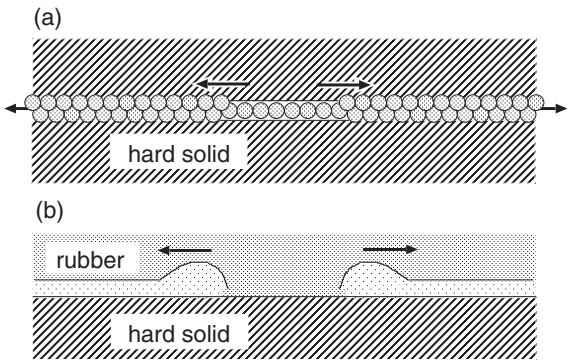


**Figure 34.** (a) Squeeze-out of a fluid between hard solid walls. During the layering transition $n \to n-1$ ($n = 2$ in the figure) the surfaces are everywhere separated by $n$ or $n-1$ monolayers of fluid. The 2D fluid velocity is non-vanishing at the periphery of the contact area. (b) Squeeze-out of a nonwetting liquid between a hard substrate and an elastically soft block. The squeezed liquid accumulates in a rim and the fluid velocity at the periphery of the contact area vanishes.

displaces as a whole toward the periphery of the contact area. Since the volume of fluid trapped between the solid walls decreases continuously during squeeze-out, there will be a pressure induced work on the film which, as shown above, is the main driving force for the squeeze-out. The pressure work is dissipated at the interface via an interfacial frictional process, which occurs when the $n$-layer 2D fluid slab moves relative to the solid walls. The balance between the 'pressure' force and the interfacial friction force determines the squeezing dynamics and the squeeze-out time; see section 4.2.

For a nonwetting liquid between elastically soft solids, e.g., rubber, another squeeze-out scenario has been observed [65–68]. Here the squeeze-out typically nucleates at some defects, e.g., a surface asperity, at a relatively large film thickness, say a few hundred ångströms, and the film thickness abruptly *vanishes* in the squeezed region; see figure 34(b). Furthermore, the squeezed fluid accumulates as a rim at the boundary between squeezed and fluid regions, and the amount of fluid between the solid walls does not change until the rim reaches the boundary of the contact area. This scenario is possible only because of the relatively small elastic energy necessary in order to deform the surrounding solid walls at the rim.

*Interfacial energies and droplet shape.* The stability of a liquid film between a rubber block and a solid substrate is controlled by the spreading parameter

$$\Delta\gamma = \gamma_{RS} - (\gamma_{RL} + \gamma_{LS}), \tag{31}$$

where $\gamma_{RS}$, $\gamma_{RL}$ and $\gamma_{LS}$ are the rubber/solid, rubber/liquid and liquid/solid interfacial free energies per unit area. If $\Delta\gamma > 0$, a liquid droplet is intercalated between the rubber and the solid, and will spread (complete wetting) at the solid/rubber interface. In this case a liquid film is stable. If $\Delta\gamma < 0$, the droplet intercalated between the rubber and the solid will not spread (partial wetting) and a flat liquid film is unstable. It is expected to dewet by nucleation and growth of a dry patch surrounded by a liquid rim, collecting the rejected liquid [5, 65–67].

The value of $\Delta\gamma$ can be derived from the static shape of a liquid droplet intercalated at the rubber/solid interface [65–67]. Thus if $H$ is the thickness of the drop and $D$ the diameter of the bottom surface (so that the contact area between the liquid droplet and the substrate $A = \pi D^2/4$), see figure 35, then the free energy of the system

$$U = -\Delta\gamma A + CE(H/D)^2 D^3 \tag{32}$$

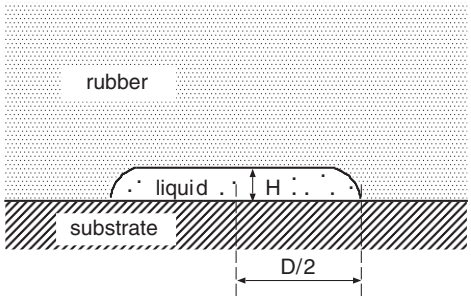


**Figure 35.** A liquid droplet trapped at the interface between an elastic solid (e.g., rubber) and a hard flat substrate.

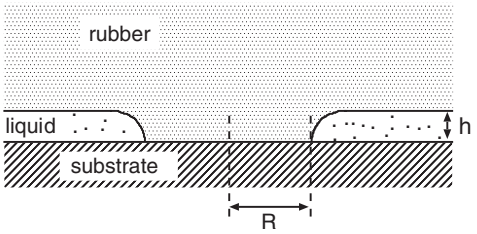


**Figure 36.** Nucleation of squeeze-out (dewetting) of a nonwetting liquid film trapped between an elastic solid (e.g., rubber) and a hard flat substrate.

where $C$ is a constant of order unity. The last term in (32) is the elastic energy stored in the rubber, which is equal to the product between the elastic modulus $E$, the square of the strain $H/D$ and the volume of the elastically deformed rubber which scales as $D^3$ with the diameter $D$. Minimizing with respect to $H$ and $D$ with the constraint that the volume $\sim H D^2$ is constant is conveniently performed using the Lagrange method. Thus with

$$U = -\Delta\gamma A + CE(H/D)^2 D^3 + \lambda H D^2$$

we get

$$\frac{\partial U}{\partial H} = 2CEHD + \lambda D^2 = 0,$$
$$\frac{\partial U}{\partial D} = -(\pi/2)\Delta\gamma D + CEH^2 + \lambda 2DH = 0.$$

Thus

$$D = \frac{6C}{\pi}\frac{H^2}{\delta}, \tag{33}$$

where the characteristic length $\delta = |\Delta\gamma|/E$ is usually in the range 100–1000 Å for soft rubber. An exact analysis [69] gives $C = \pi^2/18$. Thus from the profile of the droplet we can derive $h$ and $R$ and thus determine $\Delta\gamma$.

Let us now consider the dewetting process. Assume that the initial state consists of a uniform thick liquid layer between the substrate and the flat rubber surface. Let us first briefly discuss the nucleation of squeeze-out [65–67].

*Nucleation.* Let us estimate the free energy $U(R)$ required to make a bridge of radius $R$ between the elastomer and the solid substrate; see figure 36. The deformation of the rubber

around the contact extends over a length $\sim R$ in which the strain is of order $h/R$. Thus the stored elastic energy is $\sim E R^3 (h/R)^2$. The gain in surface energy upon forming a dry contact area of radius $R$ is $\pi R^2 \Delta\gamma$. Thus neglecting factors of order unity,

$$U \approx 2\pi R h \gamma_{\mathrm{RL}} + \pi R^2 \Delta\gamma + E R^3 (h/R)^2.$$

If we neglect the first term (which, however, is important for small enough elastic modulus $E$), since $\Delta\gamma < 0$, the function $U(R)$ correspond to a barrier with the height

$$\Delta E \approx \frac{E^2 h^4}{4\pi |\Delta\gamma|} = \frac{1}{4\pi} |\Delta\gamma| \delta^2 \left(\frac{h}{\delta}\right)^4, \tag{34}$$

and critical radius $R_{\mathrm{c}} \approx (1/2\pi) h^2/\delta$. The probability rate for nucleation of the squeeze-out is determined by the Boltzmann factor $w = \nu \exp(-\Delta E/k_{\mathrm{B}}T)$, where the prefactor $\nu$ is very large, of order $10^{16}$ s$^{-1}$, due to the large entropy associated with placing the nucleus on many different places in the contact area. For perfectly flat surfaces (no defects) nucleation on a macroscopic timescale $\tau$ (say one nucleus per second) will occur when the activation barrier $\Delta E \approx k_{\mathrm{B}}T \ln(\nu\tau) \approx 1$ eV, which for rubber ($E \approx 1$ MPa and $\Delta\gamma \approx 1$ meV Å$^{-2}$) corresponds to the film thickness $h \approx 100$ Å and the critical radius $R_{\mathrm{c}} \approx 20$ Å. In most practical applications the nucleation will occur at much larger film thickness due to imperfections.

Since $\Delta E$ must be of order 1 eV in order for the nucleation to occur on a macroscopic timescale, and since the thinnest film possible is one molecular layer (thickness $a$), equation (34) gives the highest possible elastic modulus $E = E_{\mathrm{c}}$ for which the present nucleation mechanism, involving the interfacial energy $|\Delta\gamma|$ as the driving force, is possible, namely

$$E_{\mathrm{c}} \approx \left(\frac{4\pi \Delta E |\Delta\gamma|}{a^4}\right)^{1/2} \approx 1 \text{ GPa}.$$

This is much higher than the elastic modulus of rubber, and of similar magnitude to the elastic modulus of polymers in the glassy region. However, it is much smaller than the elastic modulus of most 'normal' materials such as steel or glass, where typically $E \approx 100$ GPa. Nucleation of squeeze-out is also possible for 'hard' materials with $E > E_{\mathrm{c}}$, but in these cases the solids will not make contact in the nucleation 'hole', but will bend inward toward the hole, which reduces the elastic energy stored in the solids as a result of the applied squeezing pressure [19]. In this case the fluid, which originally occupied the region of the hole, occurs either as an in-plane density fluctuation in the monolayer film or, more probably (as assumed in the original theory [19]), the same amount of fluid is transferred to the region outside the contact area.

*Spreading.* Experiments have shown that when one of the solid walls (rubber) is elastically very soft, dewetting typically starts when the lubrication film is relatively thick, perhaps 1000 Å, when nucleation occurs at a defect [65–67]. During squeeze-out the liquid is collected into a rim that surrounds the hole. The dewetting is relatively slow (1–10 $\mu$m s$^{-1}$), and the profile of the rim is very similar to the shape of a sessile droplet. Some experimental data (see below) can be interpreted on the basis of a crude hydrodynamic model, which assumes that the gain in surface energy is entirely dissipated in the moving rim, while the rubber is purely elastic [65, 66].

Assume that $R \gg w$ and $H \gg h$, where $w$ and $H$ are the width and the thickness of the rim; see figure 37. If a dry patch of radius $R(t)$ occurs at time $t$, volume conservation of the liquid gives

$$\pi R^2 h \approx 2\pi R w H,$$

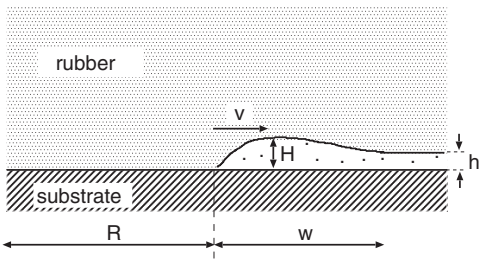


**Figure 37.** The profile of the liquid rim during squeeze-out.

or

$$Rh \approx 2wH. \tag{35}$$

If the profile of the rim is assumed to be quasistatic (i.e., similar to the profile of a sessile droplet at the solid/rubber interface), then (from equation (33) with $D = w$)

$$H^2 \approx w\delta. \tag{36}$$

Assume that the perpendicular 3D pressure is constant in the contact zone, $P \equiv P_0$. In this case the driving force for squeeze-out is entirely due to the change in the surface energy. Assuming that the gain in the surface energy is entirely dissipated in the moving liquid rim, one gets

$$\frac{\mathrm{d}}{\mathrm{d}t}(-\Delta\gamma\pi R^2) \approx \eta\left(\frac{v}{H}\right)^2 \Delta V, \tag{37}$$

where $\Delta V \approx 2\pi RwH$ is the volume of the rim, $\eta$ the fluid viscosity and $v = \dot{R}$ the velocity of the rim. In equation (37) we have neglected the elastic energy stored in the rubber at the rim since it scales as $R^{5/3}$, and is negligible for large radius $R$ of the rim. Combining equations (35)–(37) gives [65–67]

$$\frac{R(t)}{R_0} \approx \left(\frac{t}{\tau}\right)^{3/4}, \tag{38}$$

where the squeeze-out time

$$\tau = \frac{\eta}{|\Delta\gamma|}\frac{3}{4}\left(\frac{hR_0^4}{2\delta^2}\right)^{1/3}. \tag{39}$$

The prediction (38) is in good agreement with some experimental observations [66].

The assumption made above of a constant perpendicular 3D pressure is usually not a good approximation. Rather, in most cases of interest the pressure profile is nearly Hertzian, $P = P_{\mathrm{H}}(r)$. In this case there will be another contribution to the driving force for squeeze-out coming from the variation in the pressure energy as the rim of liquid moves toward the periphery of the contact zone [70]. Since the contribution to the change in the energy from the external pressure equals

$$U \approx P(R)\pi R^2 h - \int_0^R \mathrm{d}r\, 2\pi r P(r)h,$$

we get

$$\frac{\mathrm{d}U}{\mathrm{d}t} = P'(R)\pi R^2 h\dot{R}. \tag{40}$$

Assuming a Hertzian contact pressure distribution gives

$$P'(R) = -P_0 \frac{3R}{2R_0^2}\left[1 - \left(\frac{R}{R_0}\right)^2\right]^{-1/2},$$

where $R_0$ is the radius of the contact area and $P_0$ the average squeezing pressure. Thus,

$$\frac{\mathrm{d}U}{\mathrm{d}t} = -\frac{3\pi}{2} P_0 h R \dot{R}\left(\frac{R}{R_0}\right)^2\left[1 - \left(\frac{R}{R_0}\right)^2\right]^{-1/2}. \tag{41}$$

Let us compare this with the rate of change of the interfacial energy

$$\frac{\mathrm{d}}{\mathrm{d}t}(-\Delta\gamma\pi R^2) = -\Delta\gamma 2\pi R\dot{R}.$$

Since typically $(3/4)(R/R_0)^2[1-(R/R_0)^2]^{-1/2} \sim 1$ the ratio is of order

$$|\Delta\gamma| : P_0 h.$$

Since typically $|\Delta\gamma| = 0.01$ N m$^{-1}$ and $h \approx 10^{-7}$ m we get

$$10^5 \text{ N m}^{-2} : P_0.$$

Now, if we consider a tyre on a wet rough road surface, the nominal pressure in the footprint area is of order 0.5 MPa and, since the area of real contact may be only 5% of the nominal contact area, the pressure in the asperity contact areas may be 10 MPa. This is about 100 times higher than the contribution from the surface energy and we conclude that in most practical applications the surface energy term gives a negligible contribution to the driving force for squeeze-out. In this case, if the nucleation of the squeeze-out occurs in the centre of the contact area (radius $R_0$), (37) is replaced with

$$\left(2\pi|\Delta\gamma|R + \frac{3\pi}{2} P_0 h R\left(\frac{R}{R_0}\right)^2\left[1 - \left(\frac{R}{R_0}\right)^2\right]^{-1/2}\right)\dot{R} \approx \eta\left(\frac{v}{H}\right)^2 \Delta V,$$

or

$$\frac{t}{\tau} = \frac{4}{3}\int_0^{R/R_0} \mathrm{d}r\, \frac{r^{1/3}}{1 + \kappa r^2(1-r^2)^{-1/2}}, \tag{42}$$

where we introduced the dimensionless parameter

$$\kappa = \frac{3}{4}\frac{P_0 h}{|\Delta\gamma|}. \tag{43}$$

In figure 38 we show the radius $R$ of the squeezed out region (in units of the radius of the contact area $R_0$) as a function of the squeeze-out time $t$ (in the natural unit $\tau$) for several values ($\kappa = 0, 1, \ldots, 9$) of the dimensionless parameter $\kappa$. In the measurements of Brochard-Wyart *et al*, $\kappa \sim 1$ so that deviation from the prediction of the original theory, where the elastic deformation contribution to the squeeze-out force was neglected, will only occur for $R/R_0$ larger than ~0.5. However, in many practical applications $\kappa$ may be much larger, e.g., $\kappa \sim 100$ in the context of a tyre on a wet road (see above), and it is then necessary to use the full theory rather than the limiting formula (38).

When the long range nature of the interaction between the solid surfaces (which is usually of the van der Waals nature) is taken into account, it is also possible for a thin intercalated liquid film to dewet by amplification of long wavelength thickness modulations ('spinodal dewetting') [71]. Theoretical studies have shown that 'rubber spinodal dewetting' is limited to a range of thickness 20 Å $< h <$ 200 Å. However, the study of spinodal dewetting presented in [71] neglected the spatial variation of the squeezing pressure, and in the light of the calculation presented in this paper for the squeeze dynamics, an extension of the theoretical calculations to include the spatial variation of the squeeze pressure seems worthwhile.

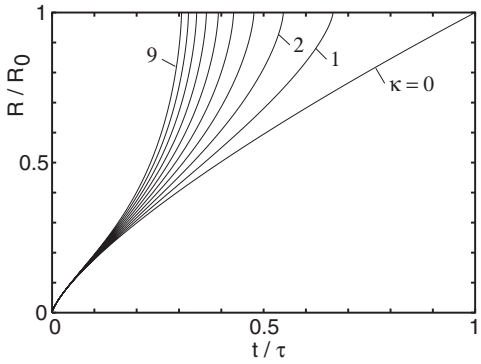


**Figure 38.** The radius $R$ of the squeezed out region (in units of the radius of the contact area $R_0$) as a function of the squeeze-out time $t$ (in the natural unit $\tau$ defined in the text). Results are shown for several values ($\kappa = 0, 1, \ldots, 9$) of the dimensionless parameter $\kappa$ defined in the text.

### *4.8. Adhesion of a soft object on a wet substrate*

The stability of intercalated liquid films is of crucial interest for many practical applications. One example is the irreversible rupture of the lachrymal film, which has been observed with silicon contact lenses: the elastomer adheres strongly to the cornea and can cause severe damage when it is removed. In contrast, when driving on a wet road, we require the water film to be squeezed away—in order to maximize grip—during the time (typically $\sim$5 ms) for which a rubber tread block stays in the footprint area. In a similar way, a living cell which comes to adhere on a substrate must eliminate the intercalated water film. The mechanism behind this *dewetting* process was discussed in section 4.7. Here we present an illustration, closely related to biological applications.

Brochard-Wyart *et al* [68] have studied the adhesion of giant vesicles of phospholipids to a glass slide. Incubated with glucose solution containing $CaCl_2$, $Ca^{2+}$ adsorbs strongly to the phosphatidylcholine head groups of the bilayer, thus conferring to the vesicles a net positive charge. Therefore they are attracted to the negative surface of bare glass at neutral pH.

The free vesicles undergo thermally excited shape fluctuations (see figure 39(a)), because they have zero surface tension (similarly to a closed plastic sack partly filled with water—the sack can take infinitely many different configurations (with the restriction of constant volume) without any cost of energy). When they adhere on the substrate, which requires the squeeze-out of the intervening water film, they become stretched and spherical (see figure 39(b)). It is clear that in biological applications similar processes may occur where the adhesion is influenced by the local chemical composition of the surrounding fluid, which can be changed, e.g., by transfer of ions into the fluid (via membrane bound ion pumps).

### *4.9. Adhesion in biological systems*

Many cells (in fluids) are able to crawl on a solid substrate to which they adhere. This motion involves, in general, three processes: the formation and protrusion of a thin lamellipod in front of the cell, the adhesion of the lamellipod to the substrate and the retraction at the rear, pulling the cell forward [73–77]. Thus, the main part of the cell body is not adhering to the substrate, e.g., a glass substrate, but is probably separated from it by a thin fluid layer. This part of the cell–substrate interface is therefore wetted by the fluid (mainly water), so that a thin fluid film intercalates between the two surfaces. However, in order for the lamellipod

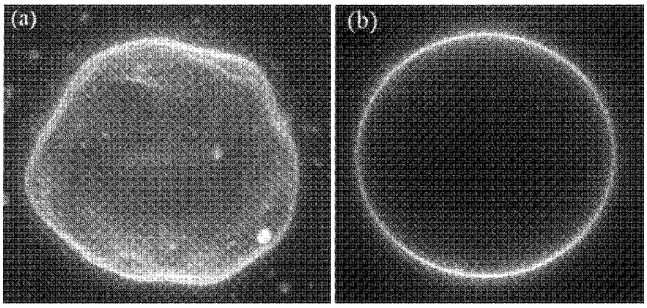


**Figure 39.** Adhesion of giant vesicles. (a) Undulations by thermal fluctuation of a free vesicle. The surface tension is zero and the surface is crumpled. (b) A tense spherical vesicle: a weak adhesion absorbs excess surface and the membrane has a surface tension. (Adapted from [68].)

to adhere to the substrate, the lamellipod–substrate interface must not be wetted by the fluid. Thus, the adhesive interaction between the lamellipod and the substrate results in a dewetting transition where the fluid is expelled from the interface. For adhesion to many biological surfaces, e.g., fibronectin, laminin or collagen, the cell utilizes integrins (special adhesion molecules located in the cell membrane). But since adhesion has been observed for many different non-biological substrates, e.g., silicone rubber or glass, there must be a non-specific contribution to the adhesive interaction, e.g., involving polar interactions and the van der Waals interaction. Thus perhaps the adhesion and dewetting transitions are initiated by changes in the concentration of molecules with ionic groups in the cell membrane, or by pumping ions between the cell and the external fluid via membrane bound ion pumps. Depending on the sign of the charged groups on the cell and on the substrate, strong adhesion or repulsion can be induced, similarly to the case of charged rubber surfaces discussed in section 3.3, or the charged vesicle discussed in section 4.8. In fact, experiments have shown that transient increase in intracellular calcium ions $Ca^{2+}$ is involved in the locomotion of fish epithelial keratocytes, and occurs more frequently in cells that become temporarily 'stuck' to the substratum, or are subjected to mechanical stretching, and in detachment of the rear cell margin [78].

The exact nature of the dewetting and adhesion process is not well understood; nor is the exact origin of how the cells can crawl on the substrate. In figure 40 we present an example of a bacterium moving on a glass substrate at a speed $\sim 8\ \mu$m min$^{-1}$. In this case the cell is propelled by an actine gel filament produced at the rear end of the bacterium, i.e., by a different (but related) mechanism to the one discussed above.

### *4.10. Droplet shape, contact angle and Laplace pressure*

As a preparation for the following two sections, let us briefly review some basic physics related to wetting and nonwetting liquids. If a small drop of a liquid is put on a substrate, the droplet will in general have the form of a spherical cup (radius $R$) with a contact angle $\theta$ (see figure 41(a)) determined by the famous Young equation:

$$\gamma \cos\theta = \gamma_{sv} - \gamma_{sl}$$

where $\gamma = \gamma_{lv}$, $\gamma_{sv}$ and $\gamma_{sl}$ are the liquid–vapour, solid–vapour and solid–liquid interfacial energies (per unit area). This equation, and the fact that the droplet takes the form of a spherical cup, both result from the minimization of the surface free energy, under the constraint that the volume of the droplet is fixed. For a wetting liquid the contact angle $\theta = 0$, so that a wetting liquid droplet will spread out on the surface, forming a uniform thin film. Since most real

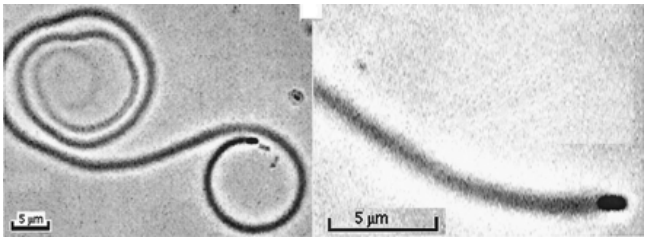


**Figure 40.** To move within cell cytoplasm and spread from cell to cell through the cytoplasmic membrane, the listeria bacterium induces the assembly of a tail, which is an actine gel made of cross-linked filaments and which forms a tubular structure. (Adapted from [72].)

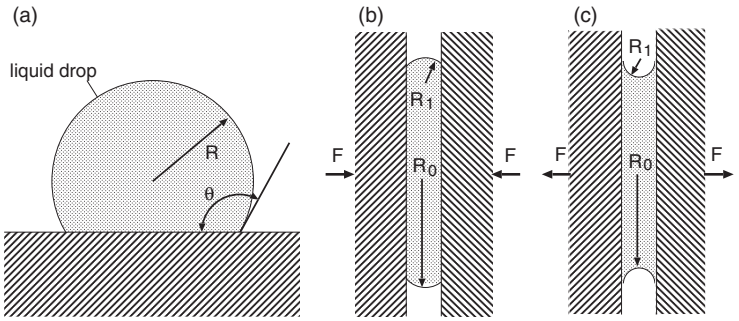


**Figure 41.** (a) A liquid droplet on a flat substrate. The drop forms a spherical cup with the radius of curvature $R$ and the contact angle $\theta$. (b) A liquid (nonwetting) drop squeezed between two solid surfaces; in this case $R_0$ and $R_1$ are both positive. (c) A wetting liquid drop between two solid walls. In this case $R_1$ is negative and a finite pulling force is necessary in order to avoid the solids being pulled together.

surfaces have defects, if a lateral force is applied to the droplet, e.g., by tilting the substrate (gravitational force), the droplet will in general not move until a critical lateral force acts on the droplet. Thus, the droplet is in general *pinned* to the substrate.

The pressure in the liquid drop in figure 41(a) is higher than the surrounding (e.g., atmospheric) pressure. This follows directly from the fact that the surface of the droplet has a curvature. The pressure increase is given by the Laplace formula

$$P = P_{\text{ext}} + 2\frac{\gamma}{R},$$

where $P_{\text{ext}}$ is the external pressure. In a more general case the surface of the liquid is not spherical, but is characterized by the radii of curvature (along the principal directions) $R_0$ and $R_1$. In this case

$$P = P_{\text{ext}} + \gamma\left(\frac{1}{R_0} + \frac{1}{R_1}\right).$$

In this formula $R_0$ and $R_1$ are positive if the origin of the radius of curvature is inside the liquid, and otherwise negative. Thus, in figure 41(b) $R_0$ and $R_1$ are both positive and a finite squeezing force must be applied to the solid walls in order for the configuration shown in the figure to be stable. In figure 41(c) $R_0$ is positive but $R_1$ is negative, and since $1/|R_1| \gg 1/R_0$, a finite pulling force must be applied to the solid walls in order for the configuration shown in the figure to be stable.

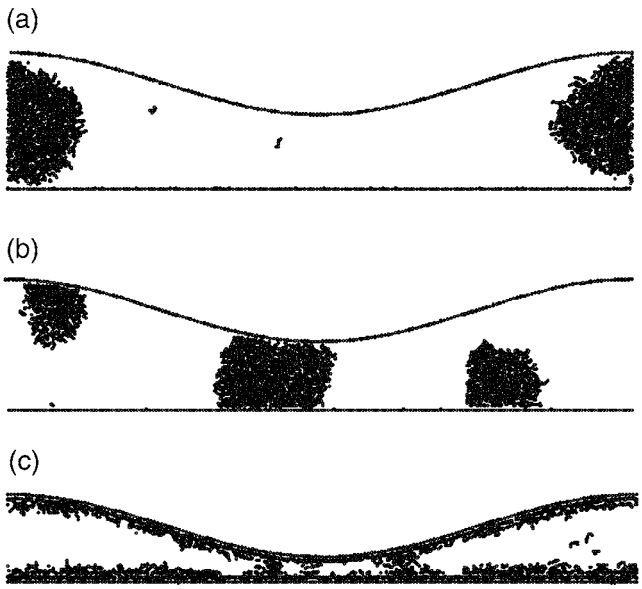


**Figure 42.** The nature of octane between two solid elastic walls, for three different cases corresponding to nonwetting (cases (a) and (b)) and wetting (case (c)). The bead–wall atom interaction energy parameter was (a) 1 meV, (b) 3 meV and (c) 18.6 meV.

### *4.11. Squeezing wetting and nonwetting fluids films*

The influences of wetting and nonwetting liquids on adhesion are paradoxical. When contacting solids are completely surrounded by a wetting liquid, the bond between the surfaces will be broken, while a nonwetting liquid may strengthen the bond. However, when a small amount (e.g., film a few molecular layers thick) of liquid occurs at the interface between the solids, it may have the *opposite* effect (see below). This fact is often made use of in nature, and in engineering applications. For example, some insects inject a very thin film of a wetting liquid at the interface between the attachment organs and the (usually rough) substrate in order to increase adhesion. On the other hand, in hair-care applications the hair fibres are covered by a thin (monolayer) hydrophobic coating, which results in effective repulsion between semi-wet (or moist) hair fibres; see section 4.12. Another well known example is the influence of water on the adhesion between sand particles: because of surface roughness, the adhesion between dry sand particles is usually very small. However, moist sand particles can adhere with measurable strength, as utilized by children when building sandcastles (note: sand particles usually have polar surfaces which are wetted by water). Finally, when sand is completely wet (i.e., immersed in water) the adhesion is again usually very low.

In this section we study the squeezing of thin octane $C_8H_{18}$ films between elastic solid walls, with different wetting properties in relation to octane [79]. The substrate is flat while the 'block' has a cosine corrugation in the $x$-direction. The model is described in detail in section 5. We have changed the energy of interaction between the octane bead units and the solid walls, from a very small value (1 meV) corresponding to a nonwetting surface with a very large contact angle (nearly 180°; see figure 42(a)) to a high value (18.6 meV) corresponding to complete wetting (see figure 42(c)).

Figure 43 shows the variation of the average pressure during squeezing, as the block moves a distance of 24 Å toward the substrate, starting at the wall–wall separation shown in

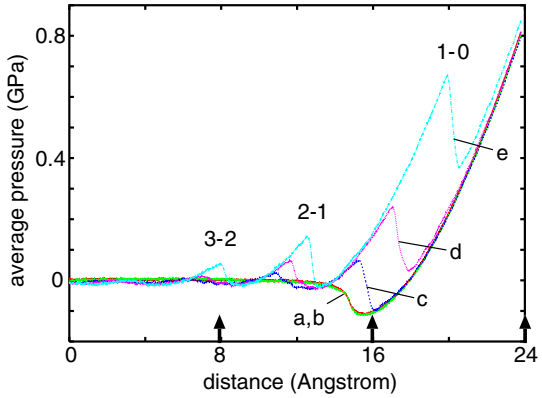


**Figure 43.** The variation of the average pressure during squeezing as the block moves a distance of 24 Å toward the substrate. Octane $C_8H_{18}$ was used as the lubricant. The squeeze velocity was $v_z = 2$ m s$^{-1}$. A symmetric pair of parameters $\epsilon_1 = \epsilon_2$ was used here equal to (a) 1 meV, (b) 3 meV, (c) 8 meV, (d) 12 meV and (e) 18.6 meV.

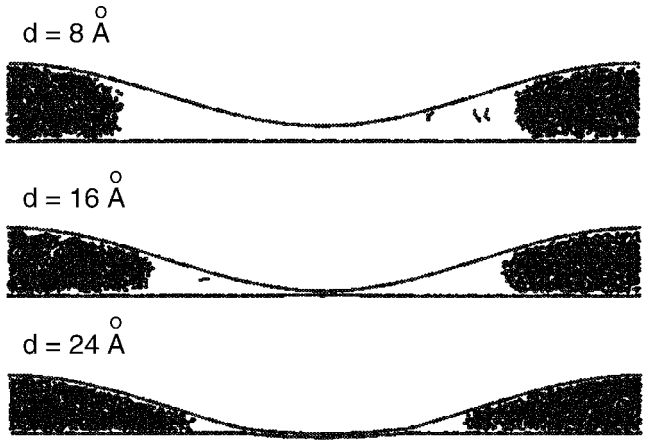


**Figure 44.** Snapshot pictures for the approach of a cosine corrugated block toward a flat substrate. Parameters $\epsilon_1 = 1$ meV and $\epsilon_2 = 1$ meV were used here. The snapshot pictures correspond to block displacements toward the substrate of 8, 16 and 24 Å.

figure 42(c). The squeeze velocity was $v_z = 2$ m s$^{-1}$. We used the same interaction energy parameters for the octane bead units and the atoms of the two solid walls, $\epsilon_1 = \epsilon_2$, equal to (a) 1 meV, (b) 3 meV, (c) 8 meV, (d) 12 meV and (e) 18.6 meV. For the system exhibiting complete wetting (zero contact angle), namely cases (c)–(e), $n \rightarrow n-1$ ($n = 3, 2, 1$) layering transitions are observed and these are indicated in the figure. For the nonwetting systems (cases (a) and (b)) no layering transitions can be observed, and, in fact, no fluid occurs in the region between the solid walls where the spacing is smallest. This is illustrated by the snapshot pictures shown in figure 44 for case (a), at the separation corresponding to the vertical arrows in figure 43. In contrast, for fluids which wet the solid walls, the fluid tends to accumulate in the region where the wall–wall separation is smallest, forming a capillary bridge. This is illustrated in figure 45 for case (e). The snapshot pictures correspond again to the block displacements $d = 8$, 16 and 24 Å, as indicated by the vertical arrows in figure 43.

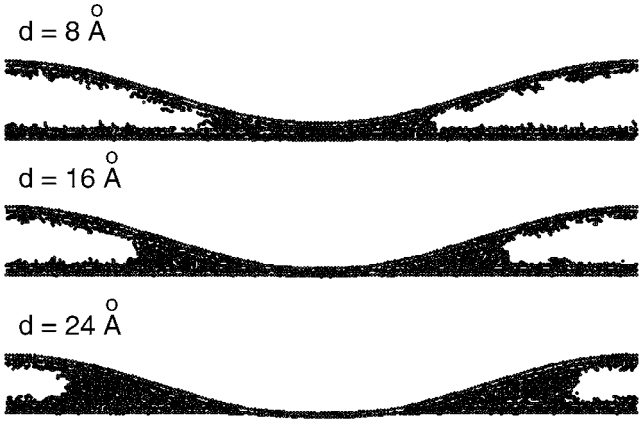


**Figure 45.** Snapshot pictures for the approach of a cosine corrugated block toward a flat substrate. Parameters $\epsilon_1 = \epsilon_2 = 18.6$ meV were used here. The snapshot pictures correspond to block displacements toward the substrate of 8, 16 and 24 Å.

Figure 42(a) shows that an octane liquid drop, when the spacing between the solid walls is large enough, forms a nearly spherical droplet in case (a). When the liquid is confined between closely spaced solid walls, there is not enough space for the droplet to take this ideal form. In order to minimize the surface energy the octane liquid is localized to the 'large' open space between the solid walls. Since the surface energy of the liquid droplet decreases as the separation between the solid walls increases (since the droplet can now take a more spherical shape), the droplet will exert a repulsive force on the solid walls. Thus, as long as the direct (attractive) wall–wall interaction can be neglected, the wall–wall interaction is repulsive. This is illustrated in figure 46 (curve (a)) (a magnified section from figure 43), which shows the average pressure acting on the block (or the substrate) as a function of the displacement of the block toward the substrate. Curve (b) in the same figure shows the (average) pressure acting on the block for the case of complete wetting, corresponding to case (e) in figure 43. In this case a capillary bridge is formed between the sold walls (see figure 45) resulting in a negative pressure acting on the block. Note that the magnitude of the negative pressure is about five times higher than the positive pressure for the nonwetting case ($\sim -10$ MPa as compared to $\sim 2$ MPa). The 'pressure peak' observed for the wetting liquid at the distance $\approx 3$ Å in figure 46(b) corresponds to the $n = 4 \rightarrow 3$ layering transition, and the strong increase in pressure around a distance $\sim 6$ Å is due to the pressure build-up before the onset of the $n = 3 \rightarrow 2$ layering transition, as is clearly seen in figure 43.

From the discussion above it is clear that if a nonwetting liquid is squeezed between solid walls with roughness (either geometrical or chemical), small liquid droplets may be trapped at the interface (see figure 47(a)), resulting in a repulsive force between the walls during squeezing, until the solid walls come into direct contact, where the wall–wall interaction may be initially attractive. This effect is made use of in some practical applications, and we will give one illustration below involving conditioners for hair-care application.

Figure 48 shows the variation of the average pressure during squeezing under the same conditions as in figure 40, except that the bead–wall interaction is now asymmetric with $\epsilon_1$ equal to (a) 1 meV, (b) 3 meV, (c) 8 meV, (d) 12 meV and (e) 18.6 meV, and with $\epsilon_2 = 18.6$ meV for all cases. In these cases, $n \rightarrow n - 1$ ($n = 3, 2, 1$) layering transitions are observed for all the systems. In figure 49 we show snapshot pictures for case (a) when the block has been

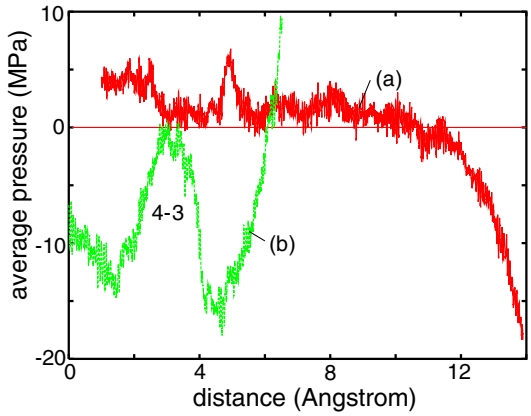


**Figure 46.** The pressure acting on the walls for (a) a nonwetting liquid and (b) a wetting liquid. For octane with $\epsilon_1 = \epsilon_2 = 1$ and 18.6 meV, respectively.

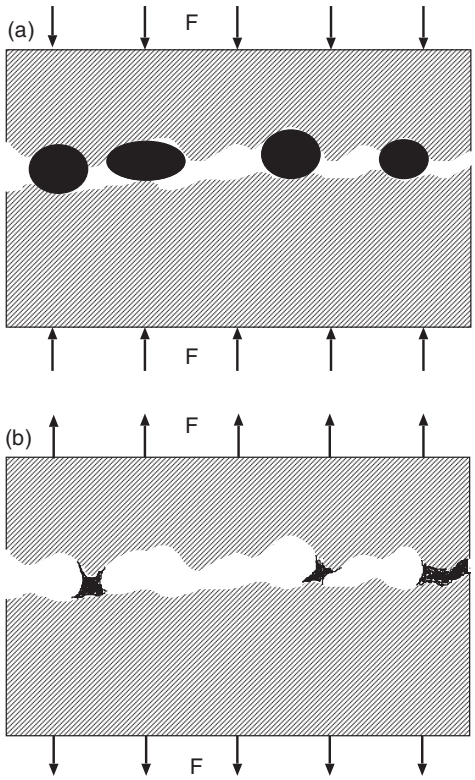


**Figure 47.** (a) A nonwetting liquid trapped between two solid walls gives rise to an effective repulsion between the walls. (b) Capillary bridges formed by a wetting liquid. In this case the liquid gives rise to attraction between the walls.

displaced toward the substrate by 8, 16 and 24 Å. For this asymmetric pair of parameters, nonwetting of the substrate surface and wetting of the block are clearly seen.

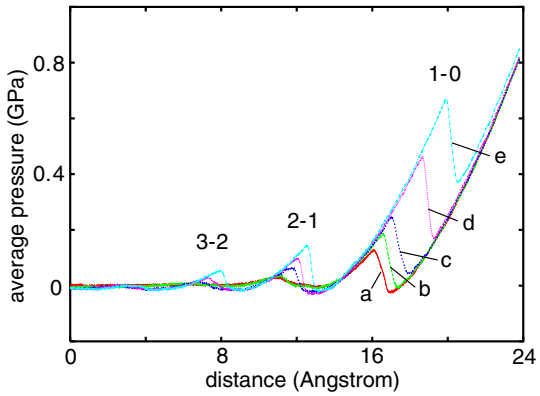


**Figure 48.** The variation of the average pressure during squeezing as the block moves 24 Å toward the substrate. For $\epsilon_1$ equal to (a) 1 meV, (b) 3 meV, (c) 8 meV, (d) 12 meV and (e) 18.6 meV and $\epsilon_2 = 18.6$ meV for all cases.


**Figure 49.** Snapshot pictures for the approach of a cosine corrugated block toward a flat substrate. Parameters $\epsilon_1 = 1$ meV and $\epsilon_2 = 18.6$ meV were used here. The snapshot pictures correspond to block displacements toward the substrate of 8, 16 and 24 Å. For this asymmetric pair of parameters nonwetting behaviour of lubricant at the surface of the substrate and wetting behaviour at the surface of the block are clearly seen.

### *4.12. A hair-care application: conditioners and the combing of wet hair*

The surfaces of clean hair fibres in water at a pH larger than ∼4 have negatively charged groups [80]. Thus when the fibres are fully immersed in water one would expect repulsive Coulomb forces to occur between the fibres, which tend to keep them separated from each other, similarly to the case of a negatively charged rubber surface in contact with a (negatively charged) glass surface, where a thin liquid layer can be trapped between the surfaces even at squeezing pressures as high as ∼0.1 MPa. Thus, completely wet hair may be relatively easily to comb. However, for semi-wet (or moist) hair, such as may result from drying the hair with a towel, the situation is different: since the contact angle for water on the clean, negatively charged, hair fibres is zero (complete wetting), capillary bridges will form in the contact areas between the hair fibres; see figure 50(b). The pressure in the capillary bridges is much lower than the surrounding atmospheric pressure, leading to strong effective adhesion between the

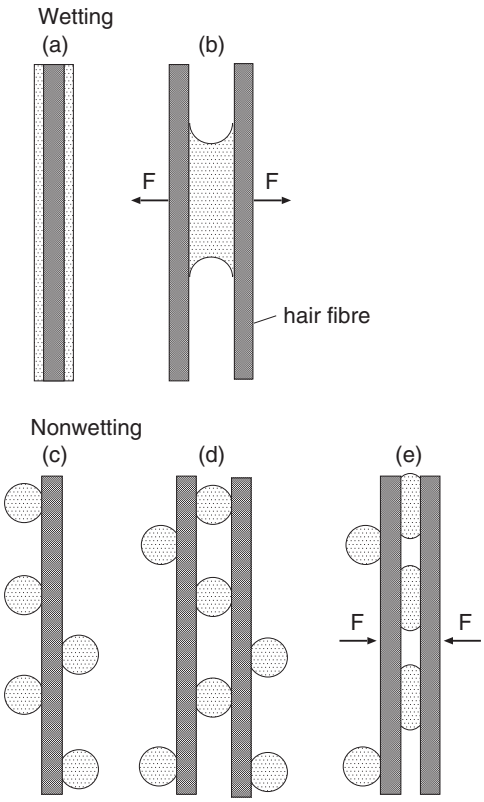


**Figure 50.** The interaction between wet hair fibres. (a) Natural (uncoated) hair fibres are hydrophilic, and coated by thin water films. (b) When two fibres come into contact, a liquid bridge is formed leading to an effective attractive interaction between the fibres. In the absence of external forces direct fibre–fibre contact will occur (not shown). (c) If the hair fibres are coated by hydrophobic monolayer films (see figure 51), the water film will break up into small droplets (dewetting transition) with nonzero contact angles to the hair fibres, determined by the interface energies (Young's law). In this case, in the absence of external forces, there is a finite natural separation between two hair fibres (see (d)). (e) At separation shorter than the natural separation, the fibres will repel each other.

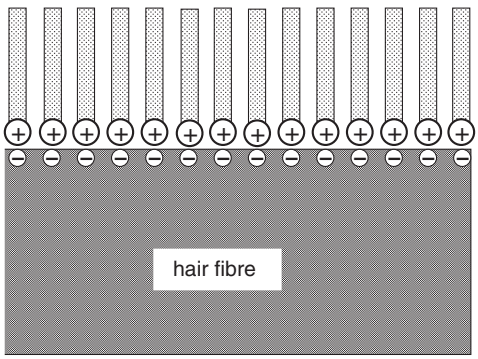


**Figure 51.** Coulomb attraction between the negatively charged hair surface and the positively charged head groups of the conditioner molecules causes head-down/tail-up adsorption at the interface.

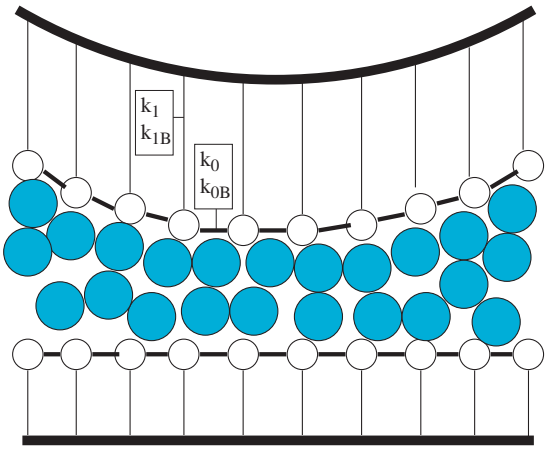


**Figure 52.** A schematic picture of the central region of the squeezing model used in the present review.

fibres. During combing of semi-dry hair, the liquid bridges will be elongated before they break, leading to an effective long range and strong attraction between the fibres, resulting in very bad combing properties. Conditioners for hair-care applications are used to reduce the combing force. These fluids contain molecules with a long hydrocarbon chain, and a *positively* charged head group, which bind strongly to the negatively charged groups on the hair fibres forming a grafted monolayer film, with the inert hydrocarbon chains pointing into the water; see figure 51. The coated hair fibres are hydrophobic with a large contact angle for water [80]. Thus, the thin water film, which may be left on the hair fibres after drying the hair with a towel, will immediately break up into small water droplets (dewetting transition). If no pinning by defects were to occur the small droplets would tend to join together into larger droplets, but due to surface defects on the hair fibres (e.g., small areas not covered by the hydrophobic monolayer film), one may expect most of the droplets to remain pinned at different locations along the hair fibres; see figure 50(c). When two hair fibres come into contact without an external squeezing force, they will be separated by a small but finite distance determined by the (average) radius of the water droplets and by the contact angle (figure 50(d)). If the fibres are squeezed toward each other, the droplets will deform as indicated in figure 50(e). (We assume here that the droplet positions are pinned so that they do not rotate or displace away from the region between the hair fibres.) Since the pressure inside the droplets is much higher than the atmospheric pressure, and since the area of contact between the droplet and the hair fibres increases during squeezing, the droplets will exert a strong repulsive force between the hair fibres. Thus, in this case the hair fibres tend to be separated from each other during combing, leading to very small fibre–fibre adhesion and friction, and good combing properties. In addition, owing to the inert nature of the monolayer film shown in figure 51, even in the absence of water the adhesion and friction between the hair fibres is reduced for hair treated with a conditioner, as compared to untreated hair.

## 5. Squeezing molecularly thin 2D solid-like films

The theory presented above is based on the assumption that the lubricant film is in a 2D fluid state. This seems to be the case in the experiments discussed above. It may also be the case for solid lubricant films during sliding. In this section we present results for lubrication films

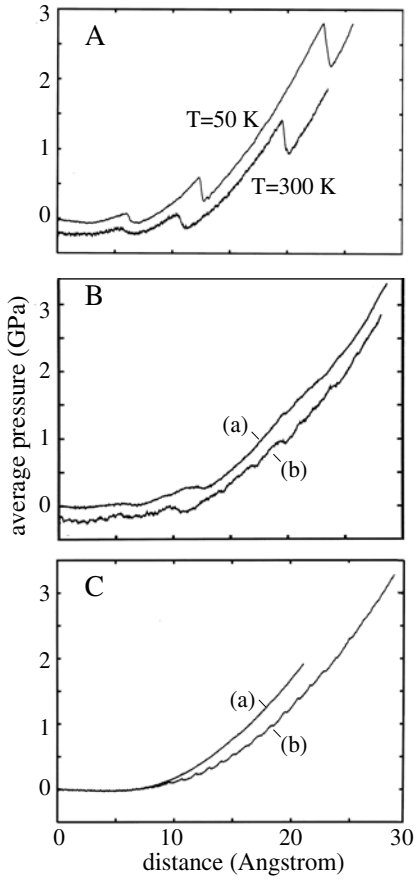


**Figure 53.** The (average) squeezing pressure as a function of the distance that the upper surface of the block has moved toward the bottom surface of the substrate, where $d = 0$ corresponds to an arbitrarily chosen point where the two surfaces with ∼4 monolayers of lubricant almost make contact. (A), (B) and (C) correspond to three different cases, where the lubricant forms (A) unpinned incommensurate, (B) pinned incommensurate and (C) strongly pinned commensurate structures. In (B) and (C), results are shown for both (a) pure squeezing and (b) squeezing and sliding. In all cases the squeezing and sliding velocities are of order a few metres per second.

which are in a 2D solid-like state. We again focus on the atomic processes by which the thickness of the interface decreases in discontinuous steps, corresponding to the decrease in the number $n$ of lubricant layers.

For solid surfaces that approach without lateral sliding, separated by unpinned or weakly pinned (incommensurate) lubrication layers, fast and complete layering transitions occur. Commensurate or strongly pinned incommensurate layers lead to sluggish and incomplete transitions, often leaving islands trapped in the contact region. As discussed above, trapped islands have been observed experimentally for 2D liquid-like lubrication films. In this latter case the island may result from dynamical instabilities of the boundary line caused by the non-linearity of the equations of motion (see section 4.3). Similar instabilities may be the origin of the trapped islands that we observe in the present case. However, when the lubrication film is in a 2D solid-like state, plastic deformation must occur during squeeze-out in order to allow different parts of the lubrication film to move with different velocities relative to the solid surfaces.

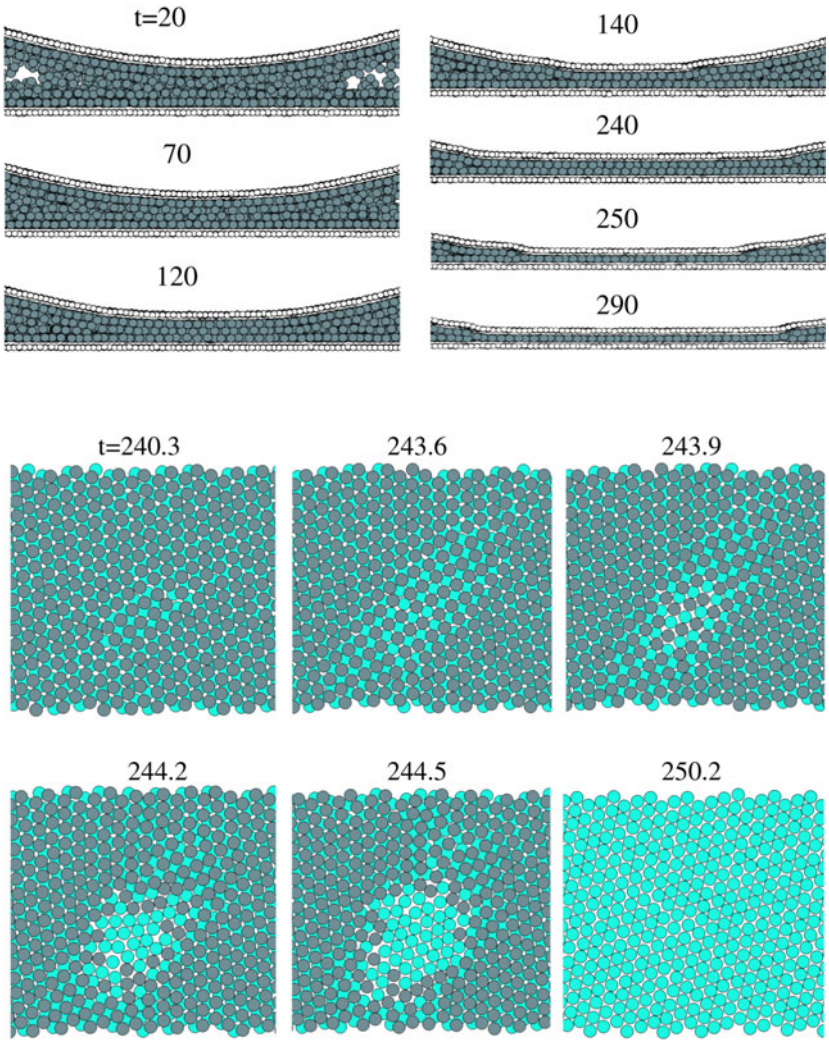


**Figure 54.** Snapshot pictures during squeeze-out. The time of each snapshot is indicated. Bottom: snapshot pictures of the lubricant layer for times close to the point where the $n = 2 \rightarrow 1$ squeeze-out transition occurs. The first- and second-monolayer atoms are indicated with different shades of grey. For model A at $T = 300$ K.

If strongly directional bonds occur between the lubrication atoms or molecules, squeeze-out may also occur by brittle fracture. This may be the case for some solid lubricants, e.g., thin graphite layers, but is unlikely to be the case for typical lubrication fluids (e.g., hydrocarbons); in the latter case the interaction between the lubrication molecules is usually of the van der Waals type, i.e., weak and undirectional, which favours local atomic rearrangements and plastic flow. For commensurate layers we observe that it is nearly impossible to squeeze out the last few layers simply by increasing the perpendicular pressure. However, the squeeze-out rate is greatly enhanced by lateral sliding, since, in this case, the lubricant film can turn into a fluidized or disordered state, facilitating the ejection of one layer.

### 5.1. Atomic lubricants

We are concerned with the properties of a lubricant film squeezed between the curved surfaces of two elastic solids. In our model, as well as in SFA experiments, a system of this type is obtained by 'gluing' two elastic slabs (of thickness $W_1$ and $W_2$) to 'rigid' surface profiles of arbitrary shape. If the radii of curvature of the rigid surfaces are large compared to $W_1$ and $W_2$, the elastic slabs will deform, reproducing with their free surfaces the (nearly arbitrary) shape of the underlying rigid profiles.

In what follows we denote the lower solid as the *substrate*, which is taken to be fixed in space. The upper solid, denoted as the *block*, will be moving. To account for the elastic response of the slabs, without dealing with the large number of atoms required to simulate a mesoscopic elastic solid, we treat explicitly, at the atomistic level, only the last atomic layer of the solids at the interface. These atoms are connected to a *rigid* curved surface (or profile). The force constants connecting these atoms to the rigid profile, however, are not the bare parameters, determined by the model interatomic potential. Instead, those force constants are treated as effective parameters that implicitly re-introduce the elastic response of the slabs of arbitrary widths $W_1$ and $W_2$.

The model is illustrated in figure 52 (see also [37, 47, 48]). The atoms in the bottom layer of the block (open circles) form a simple square lattice with lattice constant $a$, and lateral dimensions $L_x = N_x a$ and $L_y = N_y a$. Periodic boundary conditions are assumed in the $xy$ plane.

We have performed simulations for the three different cases (A)–(C). In all cases the lubricant is Xe, but we have varied the Xe–substrate lattice constant so that a monolayer film of lubrication atoms forms unpinned (case (A)) or pinned (case (B)) incommensurate layers, or a commensurate layer (case (C)).

(A) *Incommensurate layer (unpinned).* In the computer simulations, the block and the substrate are initially separated by about four Xe monolayers. The pressure–displacement curves exhibit 'bumps' corresponding to the layering transitions (with increasing pressure) $n \to n-1$ ($n = 4, 3, 2$); see figure 53(A). We observe that these transitions are rather abrupt, and are marked by a significant pressure drop. The latter implies that the squeeze-out occurs so rapidly that, during the transition, the upper surface has moved (velocity $v_z \approx 1$ m s$^{-1}$) only a small fraction of the diameter of the Xe monolayer. We observe that the layering transitions occur at higher pressures at low temperature, indicating that they are thermally activated.

Inspection of snapshot pictures of the lubrication film during the nucleation of the squeeze-out $n = 2 \to 1$ shows that immediately before the nucleation of the layering transition the lubrication film in the central region has undergone a phase transformation and now exhibits fcc(100) layers parallel to the solid surfaces. Since the fcc(100) layers have a lower concentration of Xe atoms than the hexagonal layers (assuming the same nearest neighbour Xe–Xe distance), a fraction of the Xe–solid binding energy is lost during this transformation. On the other hand the solid surfaces can now move closer to each other (since the distance between the fcc(100) layers is smaller than that between the hexagonal layers) and in this way elastic energy is released. After the phase transformation, the layering transition $n = 2 \to 1$ can occur much more easily since density fluctuations (opening up of a 'hole') require less energy in the more dilute fcc(100) layers than in the higher density hexagonal layers; see figure 54. The 'hole' in the lubrication film is stabilized by the inward relaxation of the solid walls as indicated in the snapshot pictures shown in figure 55.

(B) *Incommensurate layer (pinned).* We have studied squeeze-out both without (a) and with

(b) lateral sliding. We find, in contrast to case (A), that in the present case, where the lateral atomic corrugation experienced by the lubrication atoms is much higher, the squeeze-out is more sluggish, and only very weak bumps corresponding to the $n = 4 \rightarrow 3$ and $3 \rightarrow 2$ transitions can be detected in the pressure–displacement curve; see figure 53(B).

In case (a) it is found that at the end of squeezing, a trapped $n = 2$ island occurs, surrounded by a single Xe monolayer. This is reminiscent of the trapped islands observed experimentally for 2D liquid-like lubrication films. In this latter case the islands may result from dynamical instabilities of the boundary line caused by the non-linearity of the equations of motion. Similar instabilities may be the origin of the trapped island that we observe in the present case. However, when the 2D lubrication film is in a solid-like state plastic deformation must occur during squeeze-out in order to allow different parts of the lubrication film to move with different velocity relative to the solid surfaces. During squeezing and sliding the $n = 2 \rightarrow 1$ transition is complete, i.e., no $n = 2$ island remains trapped.

(C) *Commensurate layer.* The commensurate adsorbate layers are strongly pinned, and even though the Xe–substrate binding energy in the present case is much smaller than for case A, it is (if no lateral sliding occurs) difficult to squeeze out the lubrication film. Thus at the end of the squeeze-out process (no sliding) the surfaces are still separated by four Xe layers, just like at the beginning of squeeze-out (curve (a) in figure 53(C)). However, lateral sliding tends to break up the pinning (e.g., fluidization of the adsorbate layer may occur), and during sliding it is much easier to squeeze out the lubrication layer, and at the end of squeeze-out only one Xe layer remains between the surfaces in the high pressure region (curve (b) in figure 53(C)).

*Crack-like squeeze-out.* In some cases, at low temperature and at very high confining pressure, we have observed that the squeeze-out occurs in a sequence of very fast events similar to brittle fracture. As an example, the $t = 0$ snapshot picture (from the central region of the contact area) in figure 56 shows a trapped Xe bilayer during squeezing of Xe lubricant between two curved surfaces with a similar elastic modulus to steel. The picture is from the top of the block, and for clarity we do not show the block and substrate atoms. At the periphery of the contact area the Xe atoms form hexagonal layers: this maximizes the binding energy of Xe within the layer. However, in the central part of the contact region the Xe atoms form (relative to the block surface) a $1 \times 1$ domain wall superstructure, where the domain walls have a lower concentration of Xe atoms than in the perfect $1 \times 1$ structure. The origin of this phase transformation from hexagonal layers in the low pressure region to the domain wall superstructure is the latter structure allowing the solid walls to come closer to each other by a small distance which gives rise to a lowering of the total energy since the elastic energy stored in the walls is reduced.

The Xe atoms form commensurate $1 \times 1$ regions separated by low density domain walls. In the present case the squeeze-out occurs stepwise in a series of fast events. The first event involves the formation of a small 'hole' in the *region of a low density domain wall* as indicated by the $t = 2$ snapshot in figure 56. This hole remains for a short time period after which a rapid squeeze event occurs along a low density domain wall as illustrated in snapshot pictures $t = 26$ and 28 in figure 56. This event is very similar to a crack propagating along a grain boundary in a solid and may have a similar physical origin, involving stress concentration at the crack tip.

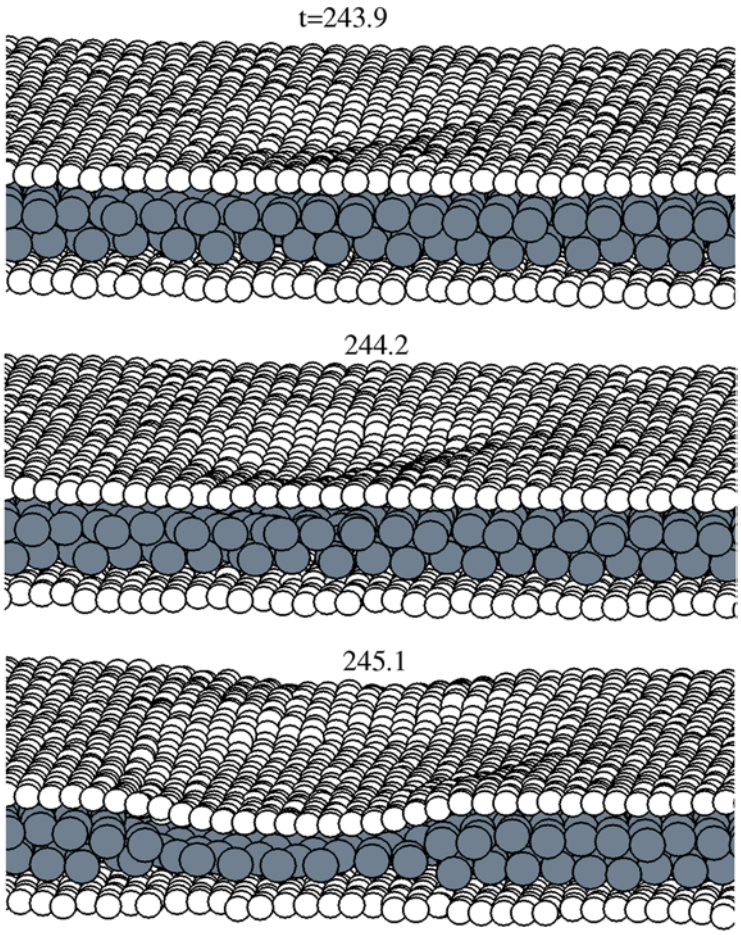


**Figure 55.** Snapshot pictures, at an inclined view angle, of the central region of the system at three time points immediately after the $n = 2 \rightarrow 1$ squeeze-out transition has nucleated. For model (A) and temperature $T = 300$ K.

### *5.2. Linear hydrocarbons*

The properties of alkane lubricants confined between two approaching solids have been investigated using the same model as above (see figure 52) [81] (see also [82]). We consider linear alkane molecules of different chain lengths, $C_3H_8$, $C_4H_{10}$, $C_8H_{18}$, $C_9H_{20}$, $C_{10}H_{22}$, $C_{12}H_{26}$ and $C_{14}H_{30}$, confined between smooth gold surfaces. We observe that well defined molecular layers develop in the lubricant film when the width of the film is of the order of a few atomic diameters. An external squeezing pressure induces discontinuous changes in the number $n$ of lubricant layers. We find that with increasing alkane chain length, the transition from $n$ to $n - 1$ layers occurs at higher pressure, as expected on the basis of the increasing wettability with increasing chain length.

We now describe the results obtained from the simulations for seven different linear alkane species as lubricants, starting from thermal equilibrium at the temperature $T = 300$ K at a point where the block and the substrate are separated by four monolayers of lubricant. The total squeezing distance is about 20 Å depending on the system considered.

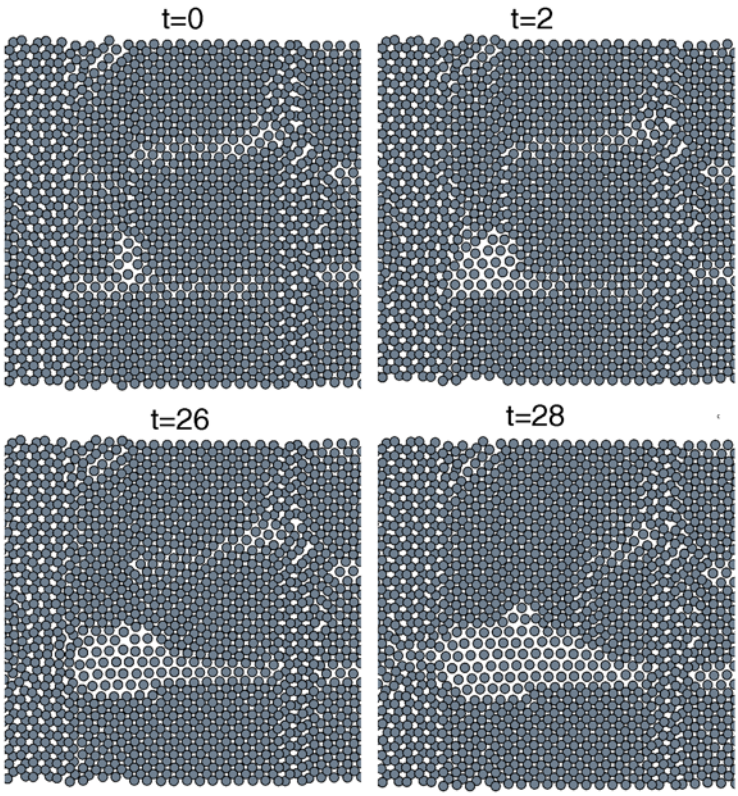


**Figure 56.** Snapshot pictures during the squeeze-out of Xe from the interface between two curved elastic solids.

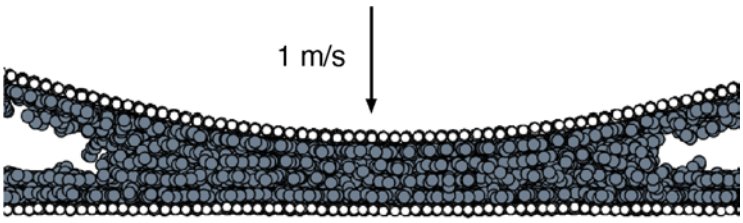


**Figure 57.** A snapshot picture during squeezing with decane as the lubricant. The squeezing velocity is 1 m $s^{-1}$. The block has moved a distance of 3 Å resulting in a film of decane four monolayers thick between the surfaces.

In order to illustrate the squeezing systems, decane ($C_{10}H_{22}$) was chosen as an example in figure 57. In this figure the arrow shows the squeezing movement of the block toward the substrate. It can be observed that the surfaces are separated by four monolayers of decane in the central region at a point where the block has moved a distance of 3 Å.

Figure 58 shows the average pressure during squeezing as a function of the distance moved by the block. Of the seven systems investigated, only propane, octane and tetradecane are shown, for clarity. Each jump in the pressure curves corresponds to a layering transition indicated by $n \rightarrow n-1$ in the figure. At about 20 Å displacement no lubricant is left between the surfaces and further movement of the block would only result in a monotonic increase in

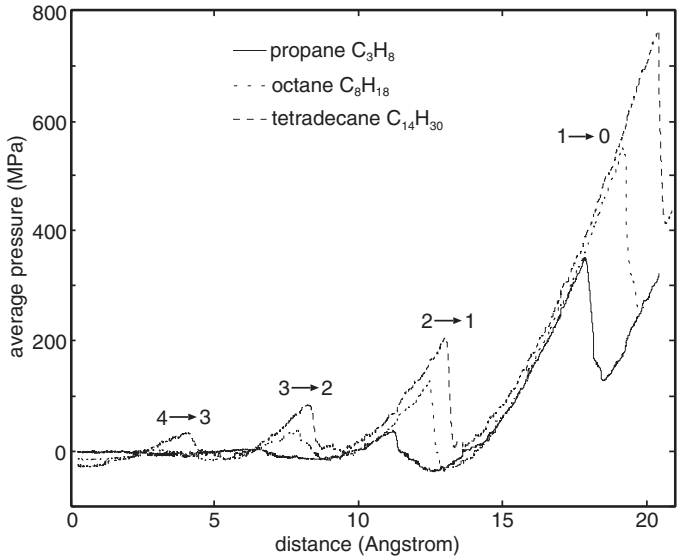


**Figure 58.** The variation of the average pressure during squeezing developed as the block moves a distance of 20 Å toward the substrate. The $n \rightarrow n-1$ layering transitions are shown for three systems: propane, octane and tetradecane.

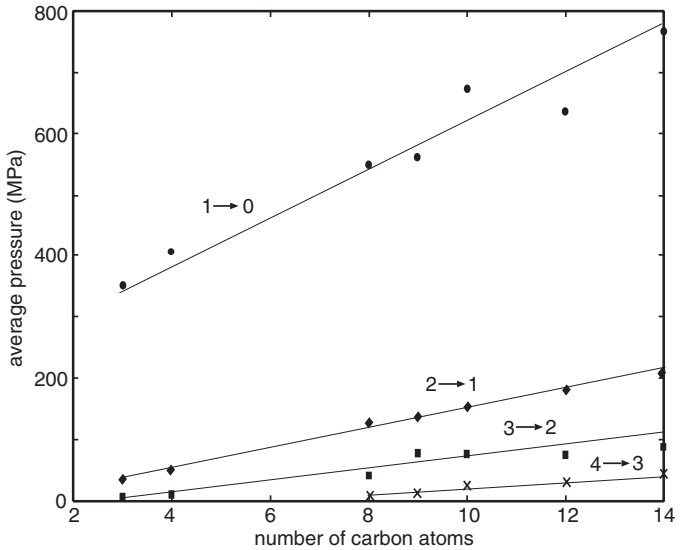


**Figure 59.** The variation of the squeeze-out average pressure during squeezing as a function of the length of the alkanes. The figure includes all the alkanes investigated. The straight lines are linear interpolation curves for the pressure at which the $n \rightarrow n-1$ layering transition occurs.

pressure. In figure 59 we show the pressure for initiating the layering transitions for all seven alkanes. Linear regression analysis is performed for each layering transition, and the resulting lines are also plotted in the figure.

We now address the question of why the long chain alkanes are better boundary lubricants than the short chain ones. We first study the lubricant film in the middle of the contact between

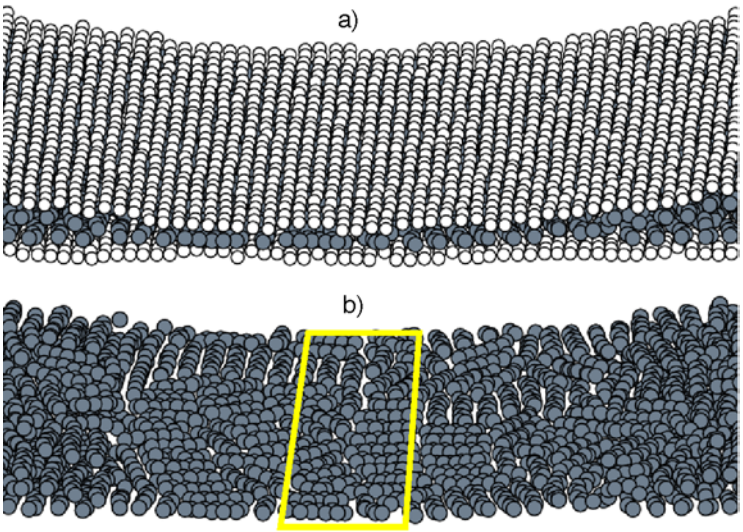


**Figure 60.** The central part of the contact between the block and the substrate. In (a) the whole system is shown whereas in (b) the surface atoms have been removed and the section displayed in figure 61 is also shown. The width is the same as the width of the contact (75.9 Å) whereas the length is 20 Å, which is 10 Å on either side of the middle of the contact.

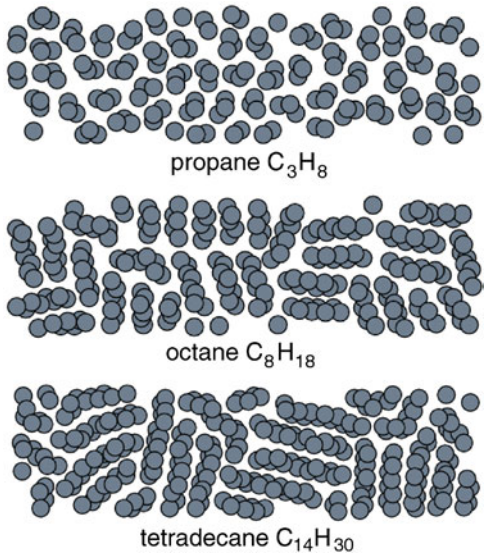


**Figure 61.** Central sections of the block–substrate contacts (see figure 60), with only the lubricant molecules shown. The alkane lubricants in this figure are propane, octane and tetradecane.

the block and the substrate. This is done at a point where all the systems have one layer left between the surfaces and where they are at almost the same average pressure.

The central sections of three systems, propane, octane and tetradecane, are shown in figure 61. From simple visual inspection of this figure, it is obvious that the density of bead units in contact with the walls increases with increasing length of the alkanes; we will now show that this results in a higher squeeze-out pressure for the long chain alkanes.

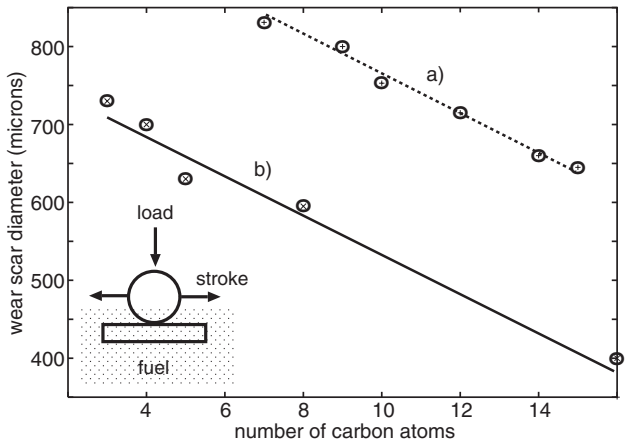


**Figure 62.** The wear scar diameter as a function of the molecule length for a number of linear alkanes. Results (a) are from [83] and (b) from [84]. The inset shows ball-on-disc configuration of a lubricity test.

Since the van der Waals lubricant–wall binding energy is roughly proportional to the number of bead units in contact with the wall, it follows that the hydrocarbon–wall binding energy *per unit area* increases with increasing chain length. At the same time the cohesive energy in the hydrocarbon liquid also increases, but at a lower rate than the hydrocarbon–wall binding energy, since the latter is usually much stronger than the binding between the hydrocarbon molecules. This is a consequence of the fact that most metals have much higher electron concentration than hydrocarbon liquids, and also more low energy electronic excitations; both effects result in a stronger van der Waals interaction energy. Thus, as the hydrocarbon chain length increases, the coefficients $a$ and $b$ in equation (8) will both increase, resulting (for fixed $c$, i.e., for fixed applied pressure) in a higher activation barrier for squeeze-out. Hence, the pressure necessary in order to nucleate the layering transition $n = 1 \rightarrow 0$ will increase with increasing chain length, in agreement with our MD computer simulations.

## 6. Relation between squeeze-out and wear

Experiments have shown that a single-monolayer lubrication film between two solid surfaces can protect against wear. We have already seen an example of this above where mica surfaces with grafted alcohol molecules can slide with low friction and without any wear. In this section we present the results of two different experiments which illustrate how wear occurs when the last lubrication monolayer has been squeezed out.

### *Steel lubricated by linear hydrocarbons*

A standard laboratory wear test is based on a ball-on-disc configuration as shown in the inset in figure 62. A steel ball oscillates on a lubricated steel disc, and the wear scar diameter on the ball is measured after a fixed number of oscillations.

Figure 62 shows wear results for surfaces lubricated by linear hydrocarbons. Trace (a) gives the wear scar diameters as a function of the number of carbon atoms in the molecules [83]. Trace (b) in figure 62 results from another recent experimental study [84]. The amounts of wear in the two experimental studies are different due to differences in the test conditions, but

in both cases the wear scar diameter decreases with increasing alkane length. The volume of steel worn off the ball is proportional to the wear scar diameter to the power four. Since the ratio of the wear scar diameters, when going from propane (3 carbon atoms) to hexadecane (16 carbon atoms) (see figure 62(b)), equals about 2, about 16 times more steel volume has been worn off in the former case.

We have shown in section 4.1 that the layering transition $n \to n - 1$ starts by a thermal fluctuation opening up a small 'hole' in the lubrication film as indicated in figure 13(a) for the $n = 1 \to 0$ transition. For a wetting liquid (as in the present case with hydrocarbons on metals or on metal oxides) the formation of a hole costs wall–lubricant binding energy and also line energy as a result of unsaturated bonds of the lubricant molecules toward the interior of the 'hole', and this results in an activation barrier $\Delta E$ to forming the 'critical' hole.

Now, the crucial observation is that the binding distance between the carbon atoms within the hydrocarbon chains ($r_{C-C} \approx 1.5$ Å) is much shorter than the van der Waals binding distance between the $CH_2$ or $CH_3$ bead units on different hydrocarbon chains, which is of order $r \approx 4$ Å. This implies, as already discussed in section 5.2, that as the hydrocarbon chain length increases, the number of bead units in direct contact with the solid walls will increase. Since the van der Waals lubricant–wall binding energy is roughly proportional to the number of bead units in contact with the wall, it follows that the hydrocarbon–wall binding energy *per unit area* increases with increasing chain length. Thus, as the hydrocarbon chain length increases, the activation barrier for squeeze-out will increase. Hence, the pressure necessary in order to nucleate the layering transition $n = 1 \to 0$ will increase with increasing chain length. Thus, long chain hydrocarbons are usually better boundary lubricants than short chain hydrocarbons, not only because of the increased viscosity which tends to increase the lubricant film thickness, but also because the squeeze-out of the last few monolayers (for which the viscosity is irrelevant and not even well defined), will, as described above, occur at higher pressure because of the better wetting (high spreading pressure) properties of the long chain hydrocarbons.

Recent wear testing [84] also included branched lubricant molecules. The linear butane and the branched iso-butane have about the same viscosity, but gave significantly different wear scar diameters, corresponding to nearly two times higher wear volume for iso-butane. This supports our relation between the wear volume and the hydrocarbon chain length, rather than the viscosity, and indicates that the surface density of lubricant atoms can be altered by changing the molecule structure. Furthermore, computer simulations have shown that molecularly thin layers of branched hydrocarbons give rise to more disordered structures than linear chains [85, 86], and that the pressure for nucleating squeeze-out decreases when disorder occurs in the lubricant film [37].

*Lubricated mica surfaces*

Sliding friction experiments (using the SFA) have been performed with molecularly smooth mica surfaces lubricated by different types of liquid. It was observed that as long as the surfaces are separated by one monolayer or more of the lubrication molecules, sliding occurs without wear [87, 88]. However, when the last lubricant monolayer has been squeezed out, wear rapidly develops. The damage which occurs during sliding is first seen as a small, highly localized, defect, and electron micrographs of the damaged region shows that a small mica flake protrudes from one of the surfaces. Damage usually occurs initially somewhere within the contact zone, but sometimes it starts at the periphery.

Once damage occurs, it propagates rapidly throughout the contact zone. Within seconds, and well before the sliding surfaces have traversed one full contact diameter (which is of order 100 $\mu$m), the surfaces are separated by a 100–1000 Å gap of wear debris (mica flakes). This scenario only applies to certain types of brittle or layered material. Thus, preliminary

experiments with silica surfaces, which are much more ductile, indicate a totally different mode of wear. It is clear that more detailed SFA studies of wear, using different solid materials, may lead to a much better understanding of the origin of wear.

## 7. Outlook

The study of the dynamics of squeeze-out of molecularly thin lubrication films between solid walls has made dramatic progress during the last few years. Thus both the nucleation and the spreading of squeeze-out are now relatively well understood for smooth surfaces. However, most surfaces of practical importance are rough with roughness on many different length scales. The detailed influence of roughness on the squeeze-out is not well understood. It is known from computer simulations that lubrication films trapped between surfaces with even a relatively small atomic roughness are much more disordered (fluid-like) than for the same lubricant between smooth surfaces, and the squeeze-out occurs in a more continuous manner. However, more detailed studies are necessary in order to gain insight into this important problem. Similarly, very little is known about the dewetting at soft interfaces when (at least) one of the walls has roughness on many different length scales. This problem may be of very high practical importance, e.g., in the context of squeeze-out of water film at the tyre–road interface or between wiper blades and glass windows.

The influence of liquids on adhesion is another problem of great importance. Thus, for example, it is known that lizards can run on wet stone walls. The adhesion between the lizard toe and a dry stone wall is now known to be due to the van der Waals interaction between thin 'hair' on the lizard toe and the stone surface, which is possible only if the hair makes atomic contact with the stone surface. The same mechanism seems to operate on a wet stone wall which requires that the water layer is removed from the contact areas between the hair and the stone wall. Exactly how this squeeze-out occurs is not known today.

In most engineering applications involving moving bodies in contact, a fluid (lubricant) is used to reduce the friction and wear. A deep understanding of how wear is related to the squeeze-out is not yet reached, although we have shown above how wear may be related to the wetting properties of the lubricant fluid in some cases (see section 6). Lubrication is particularly demanding in microelectromechanical systems (MEMS) and in magnetic storage systems. In these devices the solid surfaces are usually lubricated by liquid or grafted monolayer films; if the monolayer films are squeezed out from the sliding interfaces huge wear and device failure would occur within a short time period. In addition, in MEMS devices the lubricant film also reduces the adhesion, e.g., by protecting against the formation of (water) capillary bridges (which, if formed, would increase the effective adhesion to such an extent that the surfaces could become immobile leading to catastrophic device failure) by forming a hydrophobic coating of the surfaces. It is clear that a fundamental understanding of the squeeze-out dynamics of thin trapped (liquid-like or solid-like) lubrication films is central to a large number of 'high tech' engineering applications. In addition, we hope to have shown in this review article that the topic is of great scientific interest involving beautiful physics, and that much work still needs to be done before a complete understanding can be reached.

## Acknowledgments

The research on which this review is based was carried out in cooperation with several colleagues whose names are given in the references. BP thanks Dr K Mathauer (BASF Aktiengesellschaft) and Dr J Lee for useful discussions. He also thanks BMBF for a grant related to the German–Israeli Project Cooperation 'Novel Tribological Strategies from the Nano- to Meso-Scales', the EC for a 'Smart QuasiCrystals' grant under the EC Programme

'Promoting Competitive and Sustainable GROWTH'. FM thanks T Becker for his experimental contributions. FM thanks the German Science Foundation, grant Mu 1472/2 within the priority programme 'Wetting and Structure Formation at Interfaces'. BP and FM thank the EC for support within the 'Natribo' network of the European Science Foundation.

## References

[1] Persson B N J 2000 *Sliding Friction: Physical Principles and Applications* 2nd edn (Heidelberg: Springer)
[2] Persson B N J 1999 *Surf. Sci. Rep.* **33** 83
[3] Krim J 1996 *Sci. Am.* **275** 74
[4] Meyer E, Overney R M, Dransfeld K and Gyalog T 1998 *Nanoscience: Friction and Rheology on the Nanometer Scale* (Singapore: World Scientific)
[5] de Gennes P G 1985 *Rev. Mod. Phys.* **57** 827 and references there
[6] Craig V S J, Neto C and Williams D R M 2001 *Phys. Rev. Lett.* **87** 054504
[7] Zhu Y and Granick S 2001 *Phys. Rev. Lett.* **87** 096105
[8] Zhu Y and Granick S 2002 *Phys. Rev. Lett.* **88** 106102
[9] Cottin-Bizonne C, Jurine S, Baudry J, Crassous J, Restagno F and Charlaix E 2002 *Eur. Phys. J.* E **9** 47
[10] Pit R, Hervet H and Leger L 2000 *Phys. Rev. Lett.* **85** 980
[11] Israelachvili J N 1995 *Intermolecular and Surface Forces* (London: Academic)
[12] Gee M L, McGuiggan P M and Israelachvili J N 1990 *J. Chem. Phys.* **93** 1895
[13] Gao J, Luedtke W D and Landman U 1997 *Phys. Rev. Lett.* **79** 705
[14] Tamura H, Yoshida M, Kusakabe K, Young-Mo C, Miura R, Kubo M, Teraishi K, Chatterjee A and Miyamoto A 1999 *Langmuir* **15** 7816
[15] Demirel L and Granick S 1996 *Phys. Rev. Lett.* **77** 2261
[16] Demirel L and Granick S 1998 *J. Chem. Phys.* **106** 6889
[17] Klein J and Kumacheva E 1995 *Science* **269** 816
[18] Kumacheva E and Klein J 1998 *J. Chem. Phys.* **108** 7010
[19] Persson B N J and Tosatti E 1994 *Phys. Rev.* B **50** 5590
[20] Persson B N J 2000 *Chem. Phys. Lett.* **324** 231
[21] Zilberman S, Persson B N J, Nitzan A, Mugele F and Salmeron M 2001 *Phys. Rev.* E **63** 055103
[22] Zilberman S, Persson B N J and Nitzan A 2001 *J. Chem. Phys.* **115** 11268
[23] Butt H-J and Franz V 2002 *Phys. Rev.* E **66** 031601
[24] Loi S, Sun G, Franz V and Butt H-J 2002 *Phys. Rev.* E **66** 031602
[25] Franz V and Butt H-J 2002 *J. Phys. Chem.* B **106** 1703
[26] Nikolov A D and Wasan D T 1992 *Langmuir* **8** 2985
[27] Chu X L, Nikolov A D and Wasan D T 1995 *J. Chem. Phys.* **103** 6653
[28] Kolaric B, Foerster S and Klitzing R v 2000 *Prog. Colloid Polym. Sci.* **117** 195
[29] Kolaric B, Jaeger W and Klitzing R v 2000 *J. Phys. Chem.* B **104** 5096
[30] Golan Y, Martin-Herranz A, Li Y, Safinya C and Israelachvili J N 2001 *Phys. Rev. Lett.* **86** 1263
[31] Idziak S, Koltover I, Israelachvili J N and Safinya C 1996 *Phys. Rev. Lett.* **76** 1477
[32] Israelachvili J N, McGuiggan P M and Homola A M 1988 *Science* **240** 189
[33] Raviv P L U and Klein J 2001 *Nature* **413** 51
[34] Raviv P L U and Klein J 2002 *Science* **297** 1540
[35] Dhinojwala A and Granick S 1997 *J. Am. Chem. Soc.* **119** 241
[36] Jagla E A 2002 *Phys. Rev. Lett.* **88** 245504
[37] Persson B N J, Samoilov V N, Zilberman S and Nitzan A 2002 *J. Chem. Phys.* **117** 3897
[38] Ohnishi S, Hato M, Tamada K and Christenson H K 1999 *Langmuir* **15** 3312
[39] Kohonen M M, Meldrum F C and Christenson H K 2003 *Langmuir* **19** 975
[40] Heuberger M and Zaech M 2003 *Langmuir* **19** 1943
[41] Becker T and Mugele F 2003 *Phys. Rev. Lett.* **91** 166104
[42] Drummond C and Heuberger M 2003 private communications
[43] Zhu Y and Granick S 2003 *Langmuir* **19** 8148
[44] Mugele F and Salmeron M 2000 *Phys. Rev. Lett.* **84** 5796
[45] Mugele F, Becker T, Klingner A and Salmeron M 2002 *Colloids Surf.* A **206** 105
[46] Becker T and Mugele F 2003 *J. Phys.: Condens. Matter* **15** S321
[47] Persson B N J and Ballone P 2000 *Solid State Commun.* **115** 599
[48] Persson B N J and Ballone P 2000 *J. Chem. Phys.* **112** 9524

[49] Mugele F and Salmeron M 1999 unpublished data
[50] O'Shea S and Welland M 1998 *Langmuir* **14** 4186
[51] Jarvis S, Uchihashi T, Ishida T, Tokumoto H and Nakayama Y 2002 *J. Phys. Chem.* B **104** 6091
[52] Nakada T, Miyashita S, Sazaki G, Komatsu H and Chernov A 1996 *Japan. J. Appl. Phys.* **35** L52
[53] Israelachvili J N 1986 *J. Colloid Interface Sci.* **110** 263
[54] Chan D Y C and Horn R G 1985 *J. Chem. Phys.* **83** 5311
[55] Vinogradova O I 1995 *Langmuir* **11** 2213
[56] Hamrock B J 1994 *Fundamentals of Fluid Film Lubrication* (London: McGraw-Hill)
[57] Roberts A D and Tabor D 1971 *Proc. R. Soc.* A **325** 323
[58] Roberts A D 1974 *The Physics of Tire Friction: Theory and Experiment* ed D F Hays and A L Browne (New York: Plenum)
[59] Zilberman S, Becker T, Mugele F, Persson B N J and Nitzan A 2003 *J. Chem. Phys.* **118** 11160
[60] Mugele F, Baldelli S, Somorjai G and Salmeron M 2000 *J. Phys. Chem.* B **104** 3140
[61] Mugele F and Salmeron M 2001 *J. Chem. Phys.* **114** 1831
[62] Landau L D and Lifshitz E M 1959 *Theory of Elasticity* (London: Pergamon)
[63] Tartaglino U, Persson B N J, Volokitin A I and Tosatti E 2002 *Phys. Rev.* B **66** 214207
[64] Mukhopadhyay A, Zhao J, Bae S C and Granick S 2002 *Phys. Rev. Lett.* **89** 136103
[65] Brochard-Wyart F and de Gennes P G 1994 *J. Phys.: Condens. Matter* **6** A9
[66] Martin P and Brochard-Wyart F 1998 *Phys. Rev. Lett.* **80** 3296
[67] Martin A, Buguin A and Brochard-Wyart F 2001 *Langmuir* **17** 6553
[68] Brochard-Wyart F, Buguin A, Martin P, Martin A and Sandre O 2000 *J. Phys.: Condens. Matter* **12** A239
[69] Sneddon J 1946 *Proc. R. Soc.* A **187**
[70] Persson B, Volokitin A and Tosatti E 2003 *Eur. Phys. J.* E **11** 409
[71] Martin A, Rossier O, Buguin A, Auroy P and Brochard-Wyart F 2000 *Eur. Phys. J.* E **3** 337
[72] Gerbal F, Chaikin P, Rabin Y and Post J 2000 *Biophys. J.* **79** 2259
[73] Lee J 2003 , private communication
[74] Lee J, Ishihara A, Theriot J and Jacobson K 1993 *Nature* **362** 167
[75] DeBeus E and Jacobson K 1998 *Cell Motil. Cytoskeleton* **41** 126
[76] Wang N and Ostuni E 2002 *Cell Motil. Cytoskeleton* **52** 97
[77] DiMilla P, Barbee K and Lauffenburger D 1991 *Biophys. J.* **60** 15
[78] Lee J, Ishihara A, Oxford G, Johnson B and Jacobson K 1999 *Nature* **400** 382
[79] Samoilov V and Persson B 2003 *J. Chem. Phys.* **120** 1997
[80] Lochhead R 1988 *Cosmet. Toilet.* **103** 23
[81] Sivebaek I M, Samoilov V N and Persson B N J 2003 *J. Chem. Phys.* **119** 2314
[82] Cui S, Cummings P and Cochran H 2001 *J. Chem. Phys.* **114** 7189
[83] Wei D P, Spikes H A and Korcek S 1999 *Tribol. Trans.* **42** 813
[84] Sivebaek I M, Sorenson S C and Jakobsen J 2004 to be submitted
[85] Gao J, Luedtke W D and Landman U 1997 *J. Chem. Phys.* **106** 4309
[86] Gao J, Luedtke W D and Landman U 1997 *J. Phys. Chem.* B **101** 4013
[87] Israelachvili J N 1992 *Fundamentals of Friction: Macroscopic and Microscopic Processes* ed I L Singer and H M Pollock (Dordrecht: Kluwer–Academic)
[88] Homola A M, Israelachvili J N, McGuiggan P M and Gee M L 1990 *Wear* **136** 65